Journal of Inorganic Biochemistry 190 (2019) 1–14

Contents lists available at ScienceDirect

Journal of Inorganic Biochemistry

journal homepage: www.elsevier.com/locate/jinorgbio

Manganese coordination compounds of mefenamic acid: *In vitro* screening and *in silico* prediction of biological activity

Alketa Tarushi*, George D. Geromichalos*, Dimitris P. Kessissoglou, George Psomas*

Laboratory of Inorganic Chemistry, Faculty of Chemistry, Aristotle University of Thessaloniki, GR-54124 Thessaloniki, Greece

ARTICLE INFO

Keywords:
Bioinorganic chemistry
DNA
Manganese compounds
Albumins
In silico predictive tools

ABSTRACT

The *in vitro* and *in silico* biological properties of two manganese complexes with the non-steroidal anti-inflammatory drug mefenamic acid (Hmef) in the presence or absence of salicylaldoxime (H_2sao), *i.e.* [$Mn_6(O)_2(mef)_2(sao)_6(CH_3OH)_4$] **1**, and [$Mn(mef)_2(CH_3OH)_4$] **2**, respectively, are presented in the present contribution. More specifically, the *in vitro* biological activity of the complexes was investigated by studying their affinity to calf-thymus DNA (by diverse spectroscopic and physicochemical techniques) and their binding towards bovine (BSA) or human serum albumin (HSA) (by fluorescence emission spectroscopy). Molecular docking simulations on the crystal structures of HSA and DNA, exploring *in silico* the ability of the complexes to bind to these macromolecules, were also employed in order to explain the described *in vitro* activity of the compounds. Furthermore, *in silico* predictive tools have been employed to study the properties of the most active complex **2** to act as anticancer agent, in continuation of the previously reported cytotoxic activity. It is adopted *in silico* studies on a multitude of proteins involved in cancer growth, as well as prediction of drug-induced changes of gene expression profile, protein- and mRNA-based prediction results, prediction of sites of metabolism, quantitative prediction of antitarget interaction profiles *etc.*

1. Introduction

Mefenamic acid (Hmef, Fig. 1(A)) is a non-steroidal anti-inflammatory drug (NSAID) that belongs to the anthralinic acid derivatives [1]. Hmef is mainly used as an analgesic and antipyretic agent for the effective treatment of moderate pain such as dysmenorrheal pain and migraines [2–4]. In regard to the metal-mefenamato complexes, the existing reports include crystal structures of a series of cobalt(II) [5], copper(II) [6–8], manganese(II) [9,10], nickel(II) [11], tin(IV) [12] and zinc(II) [13] complexes with mefenamato ligands in diverse coordination modes. Most of the reported metal-mefenamato compounds were more active DNA- and albumin-binders than free Hmef [5,7,8,11,13].

Manganese is among the most important trace elements because of its presence in the active centre of many redox enzymes, including oxygen evolving center, catalases, peroxidases and superoxide dismutases [14–17]. Concerning the use of manganese compounds in medicine, their presence is rather limited to MRI contrast agent Teslascan and anticancer drug SC-52608 [18]. Within the context of medicinal inorganic chemistry, the research interest for bioactive manganese compounds has been significantly increased including reports for manganese compounds exhibiting promising antibacterial [19–21], anticancer [22–24], antifungal [25] and antioxidant [26,27] activity. Furthermore, the manganese complexes with the NSAIDs diclofenac [27–29], indomethacin [29], mefenamic acid [9,10], niflumic acid [30], and tolfenamic acid [26] have been also structurally characterized.

DNA is recognized as one of the common biological targets of anticancer drugs, since one of the main mechanisms of action of the anticancer drugs is the damage of DNA [31]. Transition metal complexes may interact with double-stranded DNA: (a) *via* covalent binding; it takes place when a labile ligand of the complex is replaced by a nitrogen atom of a DNA-base, as in the case of mechanism of action of *cisplatin*, where the hydrolysis results in the displacement of the chlorido ligands and the coordination of two guanine nitrogen atoms of DNA to platinum(II), (b) through noncovalent interactions; this kind of interactions includes intercalation which occurs *via* the $\pi \rightarrow \pi$ stacking insertion of the complex in-between DNA-bases, electrostatic interactions as a result of Coulomb forces between metal complexes and the phosphate groups of DNA, and groove-binding which takes place along major or minor groove of DNA helix due to the development of van der Waals forces or hydrogen or hydrophobic bonds, and (c) *via* cleavage of the DNA double-stranded helix along and/or across the strands [32–36].

In order to understand the mode of action of potential metal-based drugs, it is necessary to study their interaction with possible biological

---

* Corresponding authors.
E-mail addresses: atarushi@chem.auth.gr (A. Tarushi), gerom@chem.auth.gr (G.D. Geromichalos), gepsomas@chem.auth.gr (G. Psomas).

https://doi.org/10.1016/j.jinorgbio.2018.09.017
Received 29 August 2018; Received in revised form 14 September 2018; Accepted 26 September 2018

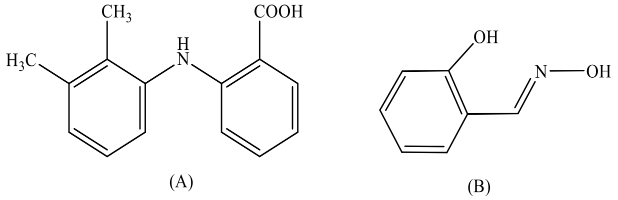

(A) (B)

Fig. 1. The syntax formula of (A) mefenamic acid (Hmef) and (B) salicylaldoxime (H_2sao).

targets including aminoacids, proteins and biomacromolecules [37]. Furthermore, the study of the interaction of NSAIDs and their compounds with DNA (which is also a biological target of the anticancer drugs) is of great importance as a first approach of their potential anti-inflammatory, antioxidant and anticancer activity [38–40].

We have already reported the synthesis, the solid-state structure, the magnetochemical properties, the spectroscopic behavior in solution and the cytotoxic effects of the hexanuclear complex $[Mn_6(O)_2(mef)_2(sao)_6(CH_3OH)_4]$ **1** (H_2sao = salicylaldoxime, Fig. 1(B)) which can be considered an *inverse*-[9-MC-3]$_2$ metallacrown (MC) and the mononuclear complex $[Mn(mef)_2(CH_3OH)_4]$ **2** [10]. The study of the interaction of the complexes with the potential biological target DNA as well as with the drug-carrier protein albumin is a first approach for further therapeutic applications. As a continuation of our previous reports [10,41], we present herein the *in vitro* study of the interaction of both complexes **1** and **2** with: (i) calf-thymus (CT) DNA by UV–vis spectroscopy and DNA-viscosity measurements as well as *via* competitive studies with the classical intercalator ethidium bromide (EB) and (ii) bovine (BSA) or human (HSA) serum albumins by fluorescence emission spectroscopy. The interaction of the complexes with CT DNA, BSA and HSA has been studied *in vitro* in order to evaluate the interaction of the complexes with biomolecules. Since drug-serum protein binding is critically involved in the manifestation of the pharmacological effects of a drug, as well as its pharmacokinetics, *in silico* approaches with the employment of molecular docking were adopted in an attempt to provide information for the understanding of the ability of both complexes in transportation through HSA and, thus, possible interaction with other protein targets involved in various diseases and especially, cancer. Additionally, a variety of computational tools were employed to predict the complete biological activity profile of the most active synthesized complex. Predictive tools include prediction of drug-induced changes of gene expression profile, protein and mRNA based prediction results, prediction of sites of metabolism, quantitative prediction of antitarget interaction profiles *etc*.

2. Experimental

2.1. Materials - instrumentation

The synthesis of complexes **1** and **2** has been already reported in our previous article [10]. CT DNA, BSA, HSA, EB, NaCl and trisodium citrate were purchased from Sigma-Aldrich Co and all solvents were purchased from Chemlab. All chemicals and solvents were reagent grade and were used as purchased without any further purification. DNA stock solution was prepared by dilution of CT DNA to buffer (containing 15 mM trisodium citrate and 150 mM NaCl at pH 7.0) followed by exhaustive stirring for three days, and kept at 4 °C for no longer than a week. The stock solution of CT DNA gave a ratio of UV absorbance at 260 and 280 nm (A_{260}/A_{280}) of 1.88, indicating that the DNA was sufficiently free of protein contamination [42]. The DNA concentration was determined by the UV absorbance at 260 nm after 1:20 dilution using $\varepsilon = 6600\,M^{-1}\,cm^{-1}$ [43]. UV–vis spectra were recorded in dimethylsulfoxide (DMSO) solution at concentrations in the range 10^{-5}–10^{-3} M on a Hitachi U-2001 dual beam spectrophotometer. Fluorescence spectra were recorded in solution on a Hitachi F-7000 fluorescence spectrophotometer. Viscosity experiments were carried out using an ALPHA L Fungilab rotational viscometer equipped with an 18-mL LCP spindle.

2.2. In vitro DNA- or albumin-binding studies

In order to study *in vitro* the interaction of complexes **1** and **2** with DNA or albumins, the compounds were initially dissolved in DMSO (1 mM). Mixing of such solutions with the aqueous buffer DNA solutions used never exceeded 5% DMSO (v/v) in the final solution, which was needed due to low aqueous solubility of the compounds. The interaction of the compounds with CT DNA was investigated by UV–vis spectroscopy and viscosity measurements and *via* the evaluation of the EB-displacing ability of the complexes studied by fluorescence emission spectroscopy. The albumin binding studies were performed by tryptophan fluorescence quenching experiments. Detailed procedures regarding the study of the biological activity of the compounds are given in the Supporting information (Sections S1–S4).

2.3. In silico computational methods and predictive tools

2.3.1. Molecular modeling and docking calculations

Preparation of complexes **1** and **2** as well as the definition of the docking parameters are given in the Supporting information (Section S5).

Virtual target screening was adopted in order to computationally screen one selected compound against a collection of virtual protein structures, to determine if a particular protein would be a potential target of a compound of interest.

2.3.2. Prediction of activity spectra

Understanding chemical-biological interactions is rather a complicated task because of the multifaceted structure-function relationships in biological systems. Prediction of activity spectra for substances (PASS) project encompasses a computational tool being able to predict the complete biological activity profile of drug-like compounds [44]. PASS may be used to estimate general pharmacological potential of compounds under study. Since computing is carried out based on a structural formula, the prediction may be obtained for compounds that are just designed on the computer, neither synthesized nor tested yet [45]. Based on prediction, one may select which of the proposed structures are the most promising ones for a particular purpose. The PASS estimates the probable biological activity profiles for compounds under study based on their structural formulae presented in MOLfile or SDF file format. General list of predictable biological activities consists of over 6400 terms including pharmacotherapeutic effects (*e.g.* antiarrhythmic), biochemical mechanisms (*e.g.* cyclooxygenase 1 inhibitor), toxicity (*e.g.* carcinogenic), metabolism (*e.g.* CYP3A4 inhibition), gene expression regulation (*e.g.* VEGF expression inhibition), transporter-related activities (*e.g.* P-glycoprotein substrate). PASS prediction is based on the knowledge base about structure-activity relationships for > 313,000 compounds with known biological activities.

2.3.3. Quantitative prediction of antitarget interaction profiles

GUSAR antitarget prediction *in silico* tool is a software for the establishment of prediction antitarget interaction profiles for chemical compounds [46]. The quantitative structure-activity relationship (QSAR) models used a set of thirty-two end-points (IC_{50}, Ki and Kact) including the data of about 4,000 chemical compounds interacting with 18 antitarget proteins (13 receptors, 2 enzymes and 3 transporters). The superiority of GUSAR performance in creating QSAR models has been shown in comparative studies with some other popular computational methods [47,48].

2.3.4. Drug-induced gene expression profiles prediction

Prediction of drug-induced changes of gene expression with Drug-Induced Gene Expression Profiles Prediction (DIGEP-Pred) *in silico* tool is based on PASS technology and two training sets created on the basis of data on drug-induced changes of gene expression profiles retrieved from Comparative Toxicogenomics Database (CTD) [49]. The gene expression changes can be considered as a particular type of the biological activity of a drug. The probability "to be active" (Pa) estimates the chance that the studied compound belongs to the sub-class of active compounds (resembles the structures of molecules, which are the most typical in a sub-set of "actives" in PASS training set). The probability "to be inactive" (Pi) estimates the chance that the studied compound belongs to the sub-class of inactive compounds (resembles the structures of molecules, which are the most typical in a sub-set of "inactives" in PASS training set).

2.3.5. Sites of metabolism prediction

The sites of metabolism prediction (SOMP) [50] is an *in silico* tool for the prediction of SOMs for drug-like compounds for (five major human) cytochrome P450s: CYP1A2, CYP2C9, CYP2C19, CYP2D6 and CYP3A4. Also in the training set, the sites of glucoronidation catalyzed by UGT were included. It is based on PASS technology and Labelled Multilevel Neighborhoods of Atoms (LMNA) descriptors. A set of all possible structures with one labeled atom (SoLAs) with the appropriate LMNA descriptors is generated for a new compound under the prediction of sites of metabolism (SOMs). The results of prediction of SOMs for new compounds are created on the basis of the prediction results of all SoLAs generated for a compound. Each SoLA relates to one appropriate SOM. For every SoLA the following values calculate the probability values P_t and P_f (P_t is the probability that labeled atom in the SoLA is the SOM of the appropriate enzyme and P_f is the probability that the labeled atom in SoLA is not the SOM of the appropriate enzyme). The atoms in compounds are arranged according to ΔP ($P_t - P_f$) values. The Invariant Accuracy of Prediction (IAP) criterion, similar to AUC (the area under the receiver operating characteristic (ROC) curve), was used to estimate the accuracy of the created method. Mathematically, IAP values equal the probability that the ΔP estimation has a higher value for a randomly selected positive example (SoLAs in which labeled atom is a SOM, $\Delta P+$) than for a randomly selected negative example (SoLAs in which labeled atom is not a SOM, $\Delta P-$): IAP = Probability ($\Delta P+ > \Delta P-$).

2.3.6. PPB for target prediction in ChEMB

In polypharmacology browser (PPB) [51], the target identification is approached with ligand-based target prediction [52–56]. Each of the target proteins is represented by set of known active ligands and targets are ranked depending upon similarity of molecule in question to the representative ligands of target proteins. PPB searches through > 1,463 targets proteins, each of which is represented by at least 20 bioactive molecules as reported in ChEMBL database. Similarity search is carried out by six different fingerprints (Topological Pharmacophore fingerprint = Xfp, Molecular Quantum Numbers = MQN, SMILES fingerprint = SMIfp, Atom-Pair fingerprint = APfp, Substructure fingerprint = Sfp, Extended-connectivity fingerprint = ECfp4) and using four combinations of parent fingerprints (Hyp1 = Xfp + SMIfp + Sfp, Hyp2 = Xfp + MQN + SMIfp, Hyp3 = Xfp + SMIfp + Sfp + ECfp4 and Hyp4 = Xfp + MQN + SMIfp + Sfp + ECfp4). For each target, P value is calculated using best match compound of "target protein" to query molecule. Bar in front of each target represents the probability which stretch from 0.01 to 0. The targets are retrieved using 6 different fingerprints and 4 combinations of fingerprints independently. Each fingerprint sorts the database according to decreasing similarity to studied compound and collects the compounds from sorted database till it finds 20 targets.

2.3.7. PharmMapper target protein identification

Top 300 targets are ranked in PharmMapper by normalized fit score in descending order. The core database consists of pharmacophore database (PharmTarget DB) containing over 7,000 receptor-based pharmacophore models (covering > 1,500 drug targets). PharmMapper identifies 'best mapping poses of the query' against all pharmacophore models in the core database.

2.3.8. Antitargets prediction and identifying DARs via the CPI

The drug repositioning and adverse reaction - chemical-protein interactome (DRAR-CPI) server [57] has a representative collection of drug molecules and targetable human proteins in drug repositioning and adverse reaction (ADR). The program is able to predict chemical-protein interactions by mining the CPI. The validation of the method is secured by matching the predictions of drug-drug associations with those predicted *via* gene-expression profiles, achieving a matching rate as high as 74%. This kind of *in silico* discovery of associations among the interaction profiles of small molecules can be efficient and cheap, and can achieve a high rate of accuracy by matching predictions to gene-expression profiles. The server uses the DOCK6 docking program [58], generating a library interactome of 254 library ligands towards 385 protein pockets in the form of a docking score matrix of 254 × 385 elements.

3. Results and discussion

3.1. Structural and spectroscopic features of complexes 1 and 2

The synthesis, structure, and solid-state and solution behavior of the complexes as well as their cytotoxic activity was recently reported [10].

In brief, the molecular structure of the hexanuclear complex **1** (Fig. 2(A)) which was determined by X-ray crystallography is constituted by two *inverse*-[9-MC-3] metallacrown cores hosting mefenamato anions. The metallacrown core contains three manganese(III) ions and three doubly deprotonated sao^{2-} ligands; the oximato oxygen (O_{ox}) and oximato nitrogen (N) of the sao^{2-} ligands are bridging two Mn(III) atoms leading to the formation of the MC ring, while the salicylato oxygens (O_{sal}) of sao^{2-} ligands participiate in the formation of a chelate ring leading to further stabilization of the MC core. An oxygen dianion (O_{cent}) is encapsulated in the cavity of each MC ring. The coordination spheres of the five- or six-coordinate manganese atoms are completed by oxygen atoms from the coordinated methanol ligands and the bidentate bridging mefenamato ligands. Considering the magnetochemical behavior of complex **1**, the complex exhibited an overall antiferromagnetic behavior.

The structure of complex **2** (Fig. 2(B)) was proposed on the basis of spectroscopic studies. The complex is mononuclear and Mn(II) is surrounded by six oxygen atoms, two oxygens from the monodentate mefenamato ligands and four ones from the methanol ligands [10].

The solution behavior of the complexes was investigated by diverse spectroscopic (UV–vis, mass) and physicochemical techniques revealing that the complexes remain practically intact in solution and keep their solid-state solution. In particular, the molar conductivity measurements indicated the non-electrolytic nature of the complexes. Although there is also the possibility of replacement of the MeOH ligands by the solvent ligands (DMSO, H_2O) where the complexes are dissolved, the NSAID ligands remain coordinated to the manganese atoms in pharmacophoric moieties $[Mn(mef)_2]$ and $[Mn_6(O)_2(NSAID)_2(sao)_6(mef)_2]$ which are responsible for the biological activity of the complexes [41]. Both complexes **1** and **2** were also tested for their *in vitro* cytotoxic effects against three cancer cell lines (HeLa, MCF-7 and A549 cells) and they presented a moderate growth inhibitory activity.

3.2. In vitro DNA-binding studies

The mode of interaction of metal complexes with double-stranded DNA is mainly dependent on the structure of the complexes and the nature of their ligands. In the case of labile ligands, covalent DNA-binding may occur, while more stable complexes may interact non-covalently with DNA in structure-dependent fashion [35,36]. Furthermore, the potential biological (antioxidant, anticancer and/or anti-

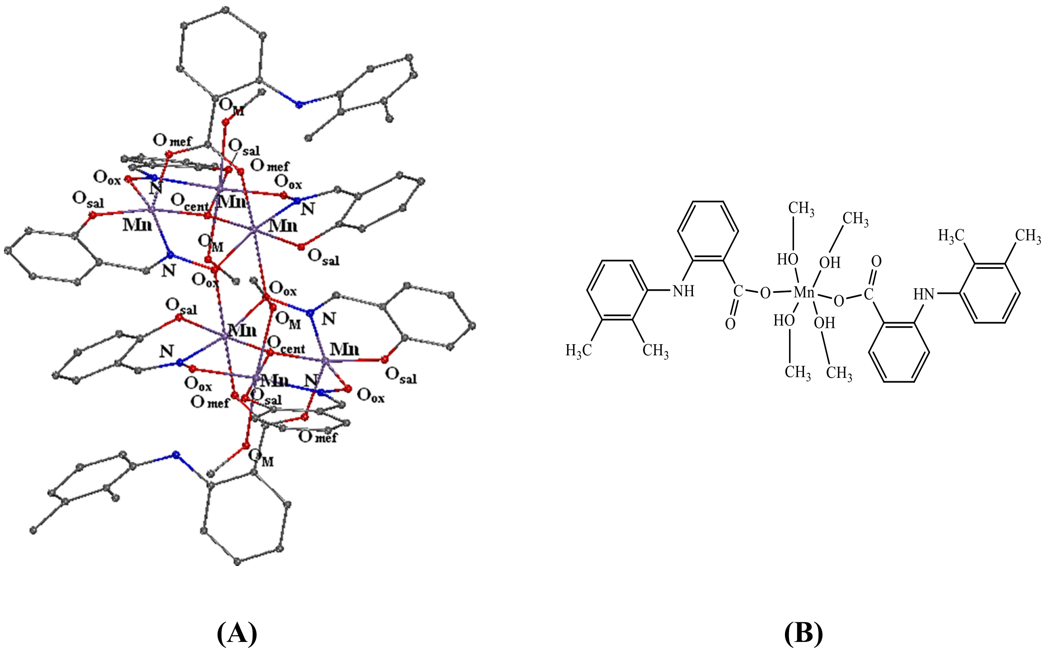

(A)

(B)

Fig. 2. (A) An illustration showing the molecular structure of complex **1**; adapted from reference [10]. (B) A sketch showing the proposed structure for complex **2**.

inflammatory) activity of the NSAIDs and their complexes has been often related to their DNA-binding ability and, thus, studies of the DNA-interaction are of increasing interest [38–41,59–61]. Within this context, the interaction of complexes **1** and **2** with CT DNA has been monitored by UV–vis spectroscopy, viscosity measurements and *via* their ability to displace a typical DNA-intercalator such as EB.

3.2.1. UV–vis spectroscopic DNA-binding studies

UV–vis spectroscopy is a used to get preliminary evidence of the DNA-binding mode and strength of the complexes. In these studies, two titrations studies are usually carried out. Initially, the UV–vis spectra of a CT DNA solution are recorded in the presence of the complexes at increasing amounts (for different *r* values) in order to verify the existence of an interaction. Afterwards, the UV–vis spectra of the compounds are recorded in the presence of CT DNA at increasing amounts in order to get a first idea of the type of the interaction and determine the strength of this interaction. The changes observed in the CT DNA band at 258–260 nm or the intra-ligand bands of the compounds may be attributed to interactions between the complexes and DNA and may provide a first approach to explain the interaction.

In the UV–vis spectra of a CT DNA solution, the DNA-band at $\lambda_{max} = 258$ nm exhibits a slight hypochromism in the presence of complex **1** at increasing amounts (Fig. 3(A)) indicating that the interaction of CT DNA with the complex may result in the direct formation of a new conjugate between DNA and complex **1** [62]. Quite similar are the changes in the UV–vis spectra of CT DNA solution in the presence of complex **2**.

In the UV–vis spectra of the complexes, the intense absorption bands which are assigned to the intraligand transitions of the NSAID ligands may be perturbed during the titration upon addition of CT DNA in diverse *r* values, if any interaction between the complex and CT DNA takes place. In the UV–vis spectra of complex **1** (10 μM), band I located at 288 nm shows upon addition of CT DNA a significant hypochromism up to 40% which is accompanied by a 14-nm red-shift (up to 302 nm), while band II located at 385 nm exhibits a more pronounced hypochromism in the presence of CT DNA leading to its elimination (Fig. 3(B)). The observed hypochromism for complex **1** accompanied by a bathochromism may be mainly attributed to $\pi \rightarrow \pi$ stacking interactions between the aromatic chromophore of the ligands of **1** and DNA-bases and is indicative of an intercalative binding mode which may lead to a stabilization of the DNA helix [63]. In the UV–vis spectra of complex **2**, the changes of the bands observed at 300 nm and 342 nm upon addition of CT DNA are not so intense to provide safe evidence regarding the DNA-binging fashion (Fig. 3(C), Table 1). The hypochromism observed for the complexes may be a preliminary indication of a possible intercalating DNA-binding mode. Further experiments, such as DNA-viscosity measurements, are necessary in order to clarify the binding mode and/or verify the existence of intercalation [64].

The DNA-binding constants (K_b, in M^{-1}) of the complexes were calculated by the Wolfe-Shimer equation (Eq. (S1)) [65] and the corresponding plots (Fig. S1). The K_b constants of complexes **1**–**2** (Table 1) are higher than that of corresponding free Hmef and are in the range reported for other metal-NSAID complexes [5,8,11,13,26–28,30,40,41,61]. The K_b constants suggest strong binding of the complexes to CT DNA, while both complexes have similar K_b constants, which are higher than that of the classical intercalator EB ($=1.23(\pm 0.07) \times 10^5\,M^{-1}$) as calculated by Dimitrakopoulou et al. [66].

3.2.2. DNA-binding studies by viscosity measurements

The measurements of DNA-viscosity upon addition of a compound may supply useful information regarding the DNA-interaction mode, because the relative DNA-viscosity (η/η_0) is sensitive to DNA-length (L/L_0) changes according to the equation $L/L_0 = (\eta / \eta_0)^{1/3}$, where L_0, L denote the apparent molecular length in the absence and presence of the compound, respectively [67]. In general, when a compound intercalates in-between DNA-bases, DNA-viscosity will increase due to the lengthening of the DNA-helix which stems from the separation of the DNA-bases in order to host the intercalating compound. In the case of partial and/or non-classic intercalation, as in DNA-grove-binding or electrostatic interactions, the DNA-viscosity is not significantly affected since such interactions may cause a bend or kink in the DNA-helix with a subsequent slight reduce of the relative DNA-length [67].

The DNA-viscosity measurements were performed on a CT DNA solution (0.1 mM) in the presence of increasing amounts of the complexes (up to the value of $r = 0.27$). The addition of compounds **1** and **2** into the DNA-solution resulted in a significant increase in the relative DNA-viscosity (Fig. 4). The observed changes of the DNA-viscosity may be attributed to the existence of intercalation between the compounds and CT DNA. This conclusion may enforce and shed light to the preliminary findings from UV-vis spectroscopic studies.

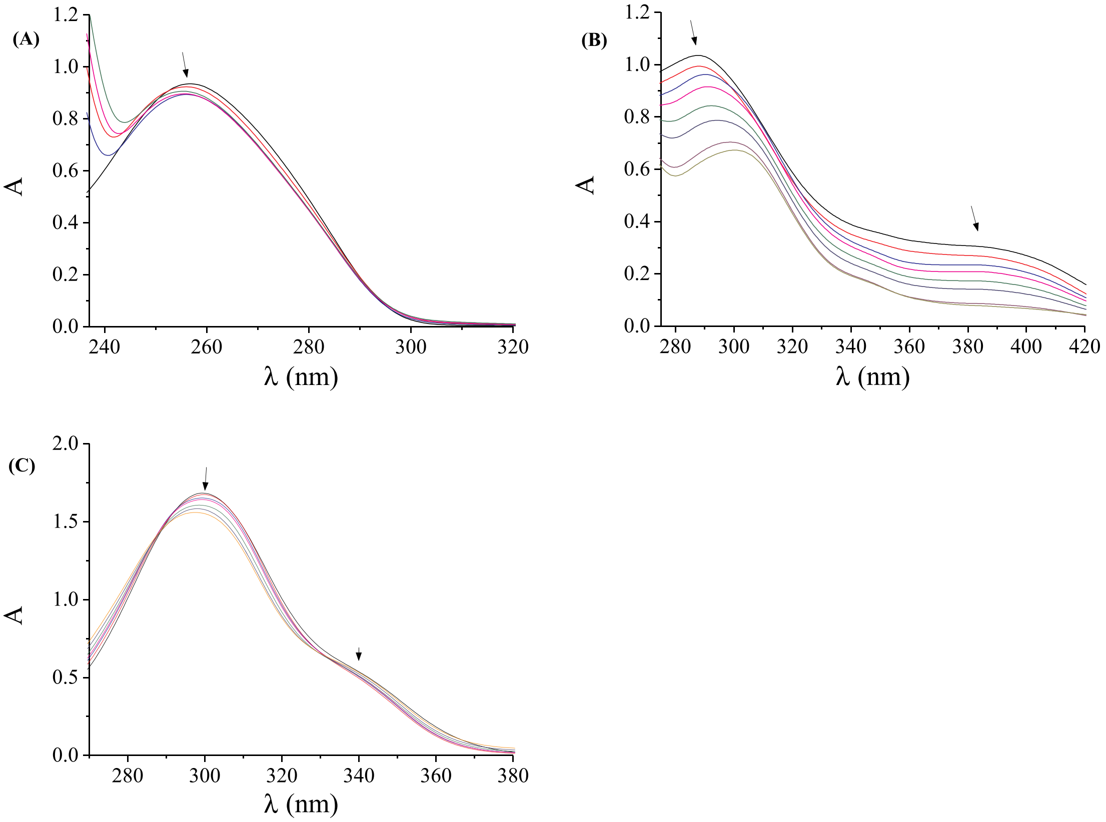

Fig. 3. UV–vis spectra of (A) CT DNA (0.14 mM) in buffer solution (150 mM NaCl and 15 mM trisodium citrate at pH 7.0) in the absence or presence of complex **1** (the arrow shows the changes upon increasing amounts of the complex), (B) complex **1** and (C) complex **2** in DMSO ([complex] = 10 μM) in the presence of increasing amounts of CT DNA (r′ = [CT DNA] / [complex] = 0–1.0, the arrows show the changes upon increasing amounts of CT DNA).

Table 1
UV-vis spectral features of the interaction of complexes **1** and **2** with CT DNA; UV-band (λ_{max} in nm) (percentage of the hyper-/hypo-chromism ($\Delta A/A_0$, %), blue-/red-shift of the λ_{max} ($\Delta\lambda$, nm)). The values of DNA-binding constants (K_b).

Compound	Band (λ, nm) (ΔA (%)[a], Δλ (nm)[b])	K_b (M^{-1})
Hmef [5]	324 (+10, 0)	$1.05(\pm 0.02) \times 10^5$
$[Mn_6(O)_2(mef)_2(sao)_6(CH_3OH)_4]$, **1**	288 (−40, +14), 385 (−55, elm[c])	$4.84(\pm 0.15) \times 10^5$
$[Mn(mef)_2(CH_3OH)_4]$, **2**	300 (−10, −1), 342 (sh) (−5, 0)	$4.60(\pm 0.26) \times 10^5$

[a] "−" denotes hypochromism, "+" denotes hyperchromism.
[b] "−" denotes blue-shift, "+" denotes red-shift.
[c] elm = eliminated.

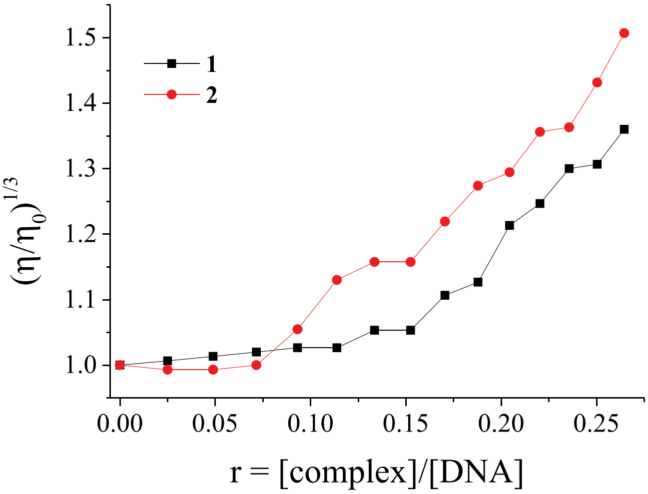

Fig. 4. Relative viscosity $(\eta/\eta_0)^{1/3}$ of CT DNA (0.1 mM) in buffer solution (150 mM NaCl and 15 mM trisodium citrate at pH 7.0) in the presence of complexes **1** and **2** at increasing amounts (*r* = [complex] / [DNA]).

3.2.3. *EB-displacement studies by fluorescence spectroscopy*

EB is a typical DNA-intercalator since its intercalation to DNA takes place *via* the insertion of the planar EB phenanthridine ring in-between adjacent DNA-base pairs resulting in the formation of an EB-DNA conjugate which presents an intense fluorescence emission band at 592 nm when the solution is excited at 540 nm. EB may be considered an indirect marker of intercalation, since the addition of another intercalating compound into the EB-DNA solution may result in a significant displacement of EB from its EB-DNA conjugate and subsequently a significant quenching of the EB-DNA emission band will appear [68,69]. Complexes **1**–**2** do not present any appreciable fluorescence emission bands at room temperature in solution or in the presence of EB or CT DNA under the same experimental conditions, *i.e.* λ_{exc} = 540 nm. Therefore, the changes observed in the fluorescence emission spectra of the EB-DNA solution compound upon addition of the complexes can be used in order to investigate the EB-displacing ability of the compounds.

The EB-DNA conjugate was completely formed after 1-h pre-treatment of EB ([EB] = 20 μM) with DNA ([DNA] = 26 μM) in buffer solution. The fluorescence emission spectra of the EB-DNA conjugate were recorded in the presence of increasing amounts of the compounds (representatively shown for complex **1** in Fig. 5(A) up to *r* = 0.2). The addition of the complexes at increasing amounts results in a significant decrease of the intensity of the emission EB-DNA band at 592 nm which

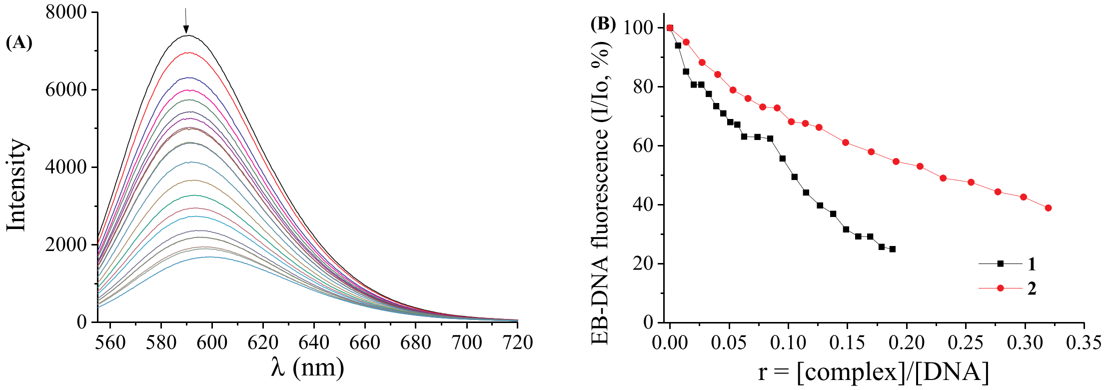

Fig. 5. (A) Fluorescence emission spectra (λ_{exc} = 540 nm) for EB-DNA ([EB] = 20 μM, [DNA] = 26 μM) in buffer solution in the absence and presence of increasing amounts of complex **1** (up to the value of *r* = 0.20). The arrow shows the changes of intensity upon increasing amounts of **1**. (B) Plot of EB-DNA relative fluorescence emission intensity (I/Io, %) at λ_{em} = 592 nm *versus r* (*r* = [complex]/[DNA]) in buffer solution (150 mM NaCl and 15 mM trisodium citrate at pH 7.0) in the presence of complexes **1** and **2** (quenching up to 24.9% of the initial EB-DNA fluorescence emission intensity for **1** and 38.9% for **2**).

Table 2

Fluorescence spectral features of the EB-displacement studies of Hmef and complexes **1** and **2**. Percentage of EB-DNA fluorescence quenching (ΔI/Io, %), Stern-Volmer (K_{SV}) and quenching constants (k_q).

Compound	ΔI/Io (%)	K_{SV} (M^{-1})	k_q ($M^{-1}s^{-1}$)
Hmef [5]	80	1.58(± 0.06) × 10^5	6.87(± 0.26) × 10^{12}
$[Mn_6(O)_2(mef)_2(sao)_6(CH_3OH)_4]$, **1**	75.1	1.69(± 0.08) × 10^5	7.35(± 0.33) × 10^{12}
$[Mn(mef)_2(MeOH)_4]$, **2**	61.1	6.10(± 0.10) × 10^4	2.65(± 0.04) × 10^{12}

is much more pronounced for complex **1** (Fig. 5(B) and Table 2). The quenching of EB-DNA fluorescence induced by the complexes may reveal that the complexes, especially **1**, present a noteworthy ability to displace EB from its EB-DNA conjugate which results from their competition for DNA-intercalation sites; thus, this quenching may indicate indirectly that the complexes interact with CT DNA in an intercalative manner [70].

The corresponding Stern-Volmer plots (Fig. S2) suggest that the observed quenching of the EB-DNA fluorescence emission band is in good agreement (R ~ 0.99) with the linear Stern-Volmer equation (Eq. (S2)) [68]. The Stern-Volmer constants (K_{SV}, in M^{-1}) of the complexes (Table 2) were obtained by the Stern-Volmer plots; the K_{SV} constants are high, they are found in the range reported for other metal-NSAIDs complexes, and complex **1** has the highest K_{SV} constant among the complexes. On the basis that the fluorescence lifetime of EB-DNA system has the value τ_o = 23 ns [71], the EB-DNA quenching constants (k_q, $M^{-1}s^{-1}$) for compounds **1** and **2** were calculated according to Eq. (S3) [68]. The k_q constants are much higher than $10^{10} M^{-1} s^{-1}$ (Table 2) indicating that the quenching of the EB-DNA fluorescence emission takes place *via* a static mechanism which leads to the formation of a new conjugate obviously between DNA and each complex [70]. Such conclusion is another indirect verification of the interaction of the compounds with DNA *via* intercalation.

3.3. *In vitro study of the interaction of the complexes with albumins*

Serum albumins (SAs) are the most abundant plasma proteins and have the role to transport metal ions, drugs and their metal complexes through the blood-stream towards the biological targets, *i.e.* tissues/organs [70]. Within this context, the interaction of potential candidate bioactive compounds with SAs is of increasing interest and should be investigated as a first approach for further applications. The solutions of HSA and its homologue BSA exhibit an intense fluorescence emission band at 352 nm and 343 nm, respectively, when excited at 295 nm, because of tryptophans, *i.e.* Trp-214 for HSA and Trp-134 and Trp-212 for BSA [67]. Since the mefenamato complexes **1** and **2** in buffer solutions do not exhibit any appreciable emission bands, when their spectra were recorded under the same experimental conditions, *i.e.* λ_{exc} = 295 nm, the quenching observed in the fluorescence emission spectra of SA solutions upon addition of the compounds may be mainly attributed to changes in protein conformation, subunit association, substrate binding or denaturation [72]. The quenching induced by the complexes to the HSA fluorescence emission band at 351 nm is moderate (for **2**) or significant (for **1**), while the quenching of the BSA fluorescence emission band at 343 nm is much more pronounced, especially for complex **1** (Fig. 6). Such intense quenching can be assigned to possible changes in protein secondary structure, thus, indicating the binding of each complex to SA [73].

The quenching constants (k_q, $M^{-1}s^{-1}$) of the complexes (Table 3) were calculated by the Stern-Volmer quenching equation (Eqs. (S2) and (S3)) [68] and the corresponding Stern-Volmer plots (Figs. S3 and S4). The obtained k_q constants are much higher than 2.0 × $10^{10} M^{-1} s^{-1}$, a value which is found for diverse kinds of quenchers for biopolymers fluorescence, and we may suggest that the interaction of the compounds with the SAs takes place *via* a static quenching mechanism which indicates the existence of a new conjugate between the albumins and the complexes [72]. These constants may indicate good SA-quenching ability, and the hexanuclear complex **1** has higher constants than the mononuclear complex **2**. In brief, the calculated quenching constants are within the range found for a series of metal-NSAIDs complexes [5,8,11,13,26–28,30,40,41,61].

The SA-binding constants (K, in M^{-1}) of the complexes (Table 3) were obtained by the Scatchard equation (Eq. (S5)) [68] and the corresponding Scatchard plots (Figs. S5 and S6). The K constants of the complexes are relatively high indicating the affinity of the complexes towards the albumins. In general, the K constants of the complexes are within the range calculated for a series of metal-NSAIDs complexes [5,8,11,13,26–28,30,40,41,61].

The K constants of the complexes are of the magnitude 10^5–$10^6 M^{-1}$; they may be considered relatively high revealing the potency of the complexes to get bound by the albumins for their potential transportation. Additionally, these values are much lower than the values of the binding constant of avidin with diverse compounds (~$10^{15} M^{-1}$) which are considered the strongest noncovalent

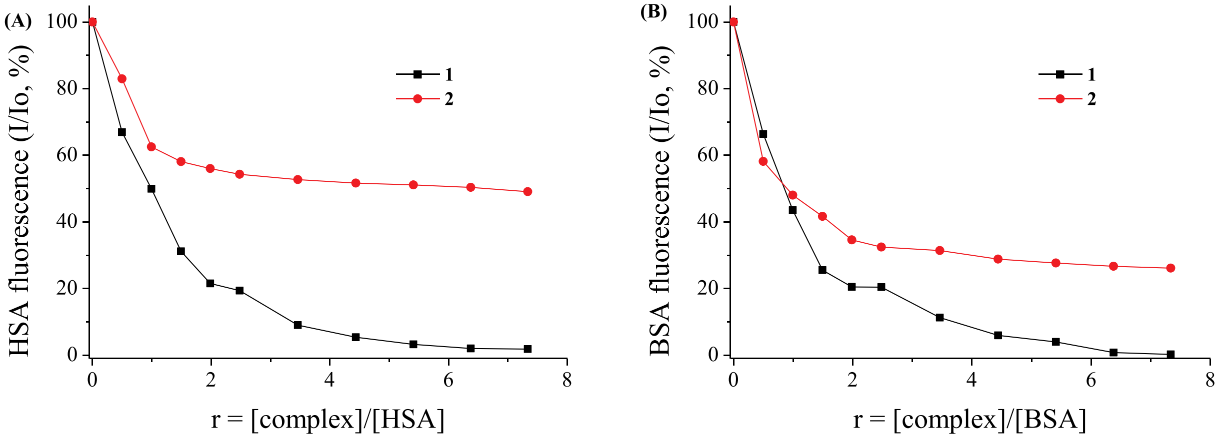

Fig. 6. (A) Plot of % relative fluorescence intensity at λ_{em} = 351 nm (%) *versus r* (*r* = [complex] / [HSA]) for complexes **1** and **2** (1.8% of the initial fluorescence intensity for **1** and 49.1% for **2**) in buffer solution (150 mM NaCl and 15 mM trisodium citrate at pH 7.0). (B) Plot of % relative fluorescence emission intensity at λ_{em} = 342 nm (%) *versus r* (*r* = [complex] / [BSA]) for complexes **1** and **2** (0.3% of the initial fluorescence intensity for **1** and 26.1% for **2**) in buffer solution (150 mM NaCl and 15 mM trisodium citrate at pH 7.0).

interactions [74]. Such comparison may suggest that the binding of the complexes to the albumins is reversible and noncovalent and reveal the ability of the complexes to get released when they are transferred successfully at their potential biological targets [74].

Table 4
Binding energies (in kcal/mol) of complexes **1** and **2** with CT DNA (pdbID: 1bna), ERa (pdbID: 1a52), ERa (pdbID: 3ert) and HSA (pdbID: 2bxg).

Complex	CT DNA	ERa (1a52)	ERa (3ert)	HSA (2bxg)
1	−13.10	−17.24	−12.98	−26.28
2	−34.57	−25.66	−34.52	−15.42

3.4. Docking calculations

3.4.1. Docking calculations on HSA

Binding energies of complexes **1** and **2** with HSA are shown in Table 4. From these data, it is obvious that complex **1** seems to succeed better binding (lower binding energy) for HSA, compared to that of complex **2**. In both docking poses, the secondary structure of HSA is shown with the subdomains color-coded in Figs. 7 and 8. The subdomains and secondary structure elements are assigned based on Sugio et al. [86]. Both complexes are shown to be stabilized inside different binding pockets of the protein, but at places which have already been reported in the literature. From Figs. 7 and 8, it is deduced that complex **2** is anchored inside binding site II more closely to ibuprofen (IBP) than complex **1**. The best (lowest energy) poses for complex **1** and IBP (in two sites) in the most common binding sites: site I, II, III, and IV in domains IA, IB, IIA, IIB, and IIIA are depicted. Complex **1** is docked in the cavity surrounded by sites I, II, III and IV (most favorable binding with lowest binding energy), while for IBP two individual poses in the binding sites III and IV are depicted. Complex **2** is anchored in binding site II, stabilized inside subdomains IB, IIB, IIA and IIIA in a pocket formed by a cluster of eight a-helices: IIIA-h4, IIB-h3, IB-h3, IIA-h1, IIA-h2, IIA-h3, IIA-h4 and IIA-h6 (Fig. 8). In total, three drug-binding sites are identified which are common with those of many other molecules crystallized with the protein.

Complex **1** is stabilized in a binding pocket formed by domains IIA, IIIA and IIB and between binding sites I, II, III and IV (Fig. 7). The involved pocket (adjacent to these of co-crystallized drug IBP) includes especially subdomain helices: IIA-h1, IIA-h2, IIA-h3, IIA-h4, IIA-h6, IIB-h3, IB-h3 and IIIA-h4. IBP is bound preferably either at binding site III in a crevice formed by domains IIA and IIB or at binding site IV formed by subdomain helices IIIA-h1, IIIA-h2, IIIA-h3, IIIA-h4, IIIA-h5 and IIIA-h6 of domain IIIA. It is interesting that subdomains IIA and IIIA are the locations for the primary fatty-acid and bilirubin-binding sites. In a close-up view of the ligand-binding pocket of HSA (Fig. 7, lower part), it is shown that complex **1** is bound in a cavity formed by the basic amino acid residues Arg160, Glu184, Glu188, Ser192, Ala191, Lys195, Lys436, Cys448, Pro447, GLu294, Val293 and Glu292.

The model for predicted binding poses of complex **2** into HSA suggests that the complex is stabilized in a cavity of the protein surrounded by regions IIA, IB, IIB and IIIA. Complex **2** is found to be anchored inside a binding cavity at binding site II, making contacts with helices IIA-h1, IB-h3, IIA-h2, IIA-h3, IIA-h4, IIA-h6, IIB-h3 and IIIA-h4. Molecular docking pose of complex **2** in the crystal structure of HSA is depicted in Fig. 8 (upper part). The key amino acid residues of the protein involved in the predicted interactions are illustrated in Fig. 8 (lower part). Since many ligands have been found to bind preferentially to IIIA, the binding cavity of this subdomain is the most active on HSA. Subdomains IIA and IIIA are the locations for the primary fatty-acid and bilirubin-binding sites. At similar positions in their structures, subdomains IIA and IIIA contain deep pockets lined with hydrophobic side chains surrounded by the first few residues of an extended loop together with helices IIIA-h5 and IIIA-h6. The entrance to the pocket in both IIA and IIIA is surrounded by positively charged amino acid residues [75]. The crystal structure of HSA shows that domains II and III share a common interface, explaining why ligands bound to domain III affect conformational changes and binding affinities in domain II. Strategically located in the hydrophobic pockets of IIA and IIIA, residues

Table 3
The albumin quenching (k_q) and binding (K) constants derived for the complexes.

Compound	$k_{q(HSA)}$ (M^{-1} s^{-1})	$K_{(HSA)}$ (M^{-1})	$k_{q(BSA)}$ (M^{-1} s^{-1})	$K_{(BSA)}$ (M^{-1})
Hmef [5]	7.13(± 0.34) × 10^{12}	1.32(± 0.15) × 10^5	2.78(± 0.20) × 10^{13}	1.35(± 0.22) × 10^5
H_2sao	1.44(± 0.03) × 10^{12}	9.12(± 0.20) × 10^3	1.94(± 0.07) × 10^{12}	9.55(± 0.01) × 10^4
Complex **1**	5.97(± 0.24) × 10^{13}	2.33(± 0.13) × 10^5	7.84(± 0.26) × 10^{13}	2.78(± 0.14) × 10^5
Complex **2**	1.26(± 0.09) × 10^{13}	8.02(± 0.26) × 10^5	3.03(± 0.17) × 10^{13}	7.19(± 0.29) × 10^5

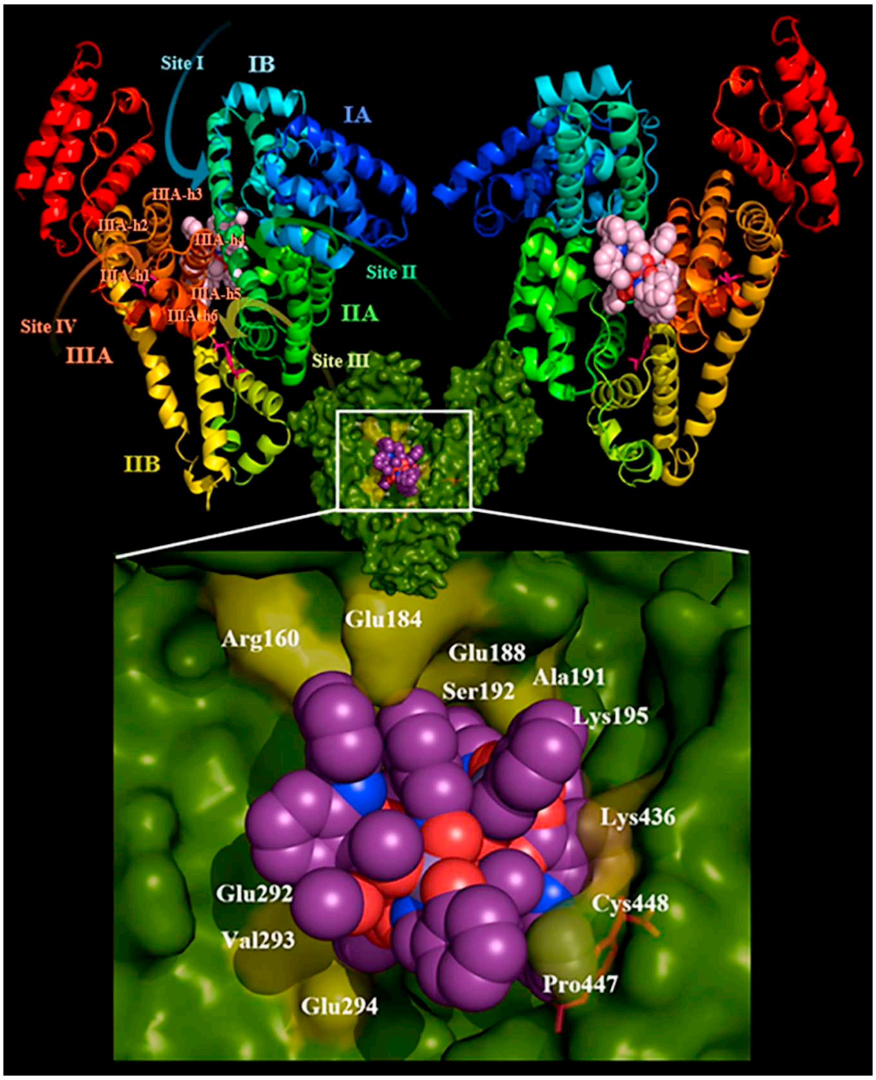

Fig. 7. Molecular docking of complex **1** (illustrated in sphere representation, light pink C atoms) and the co-crystallized drug IBP (depicted in stick model, hot pink C atoms) into HSA (Protein Data Bank (PDB) ID 2BXG) (chain A), depicting the best (lowest energy ranking) pose (upper part, left: front view, right: back view). Target protein is illustrated as cartoon with sub-domains color-coded according to chainbow. In center part, the binding pose of complex **1** (rendered in sphere model with magenta C atoms) in the protein is shown illustrated as semitransparent surface colored by chain (in green) with additional depiction of selected contacting amino acid residues of the binding pocket highlighted in yellow In lower part is shown a close up view of the binding cavity of complex **1** labeled with contacting amino acid residues. Molecular docking simulations of both compounds were performed individually. Hydrogen atoms are omitted for clarity. The final structure was ray-traced. Interacting contacts are shown in Table S2.

Trp214, Lys199, and Tyr411 are suspected by several studies to be crucial to the binding process by limiting the solvent accessibility. Molecular docking of complex **2** on HSA (Fig. 8 lower part) reported also interaction with Trp214 and Lys199 among others.

Molecular docking pose of complex **1** in the crystal structure of HSA, as depicted in Fig. 7 (lower part) and Table S2, reveals that complex **1** seems to succeed the best binding with the protein with binding interactions involving the oxygen atoms O_{sal} and O_{ox} of [9-MC-3] moiety, forming H-bond contacts with the amino acid residues of the binding cavity, as well as with the aromatic carbon atoms of H_2sao and Hmef moieties with the formation of hydrophobic contacts. From Fig. 8 (lower part) and Table S3, it is obvious that complex **2** is interacting with HSA protein mainly through mefenamato moiety, especially with the incorporation of aromatic and methyl carbon atoms forming hydrophobic contacts and, secondarily, with carboxylic and nitrogen atoms of mefenamic acid and methanolic hydroxyl groups forming H-bond contacts. Our models for HSA complexation with complexes **1** and **2** suggest that they could be bound at different sites of HSA protein, which accommodates better their transportation.

3.4.2. Docking calculations on CT DNA

The computed binding energies of the best pose of complexes **1** and **2** with CT DNA are shown in Table 4. The data propose that complex **2** can be bound more potently to DNA, than complex **1**.

From Figs. 9 and 10, it is obvious that less bulky complex **2** is inserted more deeply in minor groove than complex **1** in major groove. It is deduced that, while complex **1** is interacting with CT DNA only through one mefenamato ligand leaving its bulkier part protruding out of the major groove of DNA (Fig. 10), complex **2** interacts with DNA through both mefenamato ligands (Fig. 9), one with the phosphate group connecting DA6, DC-21 and DT-7 and one with nucleotides DG-24, DC-23 DG-2 (interrupting H-bond formed by nitrogen N2 of DG-2). The mefenamato moiety of complex **1** interacts with DA-18, interrupting the H-bond formation of N7 through H-bond networking incorporating the nitrogen atom of mefenamato moiety and wat103 molecule. Further stabilization of complex **1** is achieved through interactions with DA-17 and DG-16, and finally with nucleotides DA-18, DT-19 and DA-5 *via* an extended H-bond networking including beyond water103, also wat28 and wat91 molecules. Furthermore, the same extended H-bond networking with the inclusion of wat102 molecule is responsible for the interruption of H-bond formation between N6 of DA-5 and N7 of DG-4.

In addition, from Tables S4 and S5 illustrating the nucleotides and the atoms of the complexes involved in these binding interactions, along with bond lengths and types of interaction, it is deduced that complex **1** exhibited fewer contacts with nucleotides, compared to complex **2**, since it is anchored inside the major groove which is almost twice in width (22 Å) compared to minor groove (12 Å) in which complex **2** is docked. Lower interaction binding energy of complex **2**

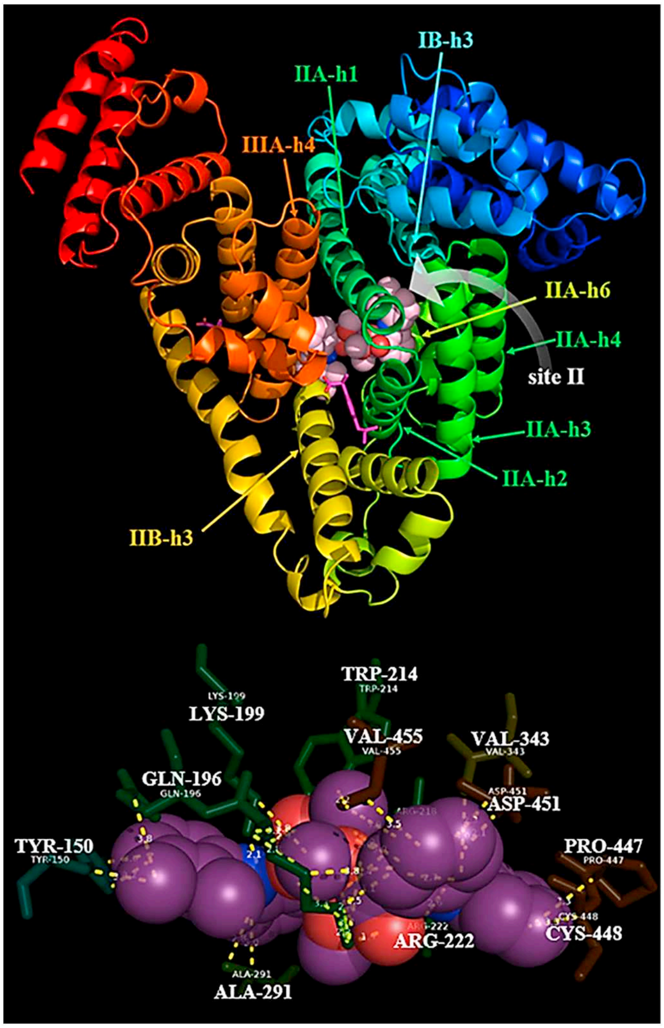

Fig. 8. Molecular docking of complex **2** (illustrated in sphere representation, light pink C atoms) and the co-crystallized drug IBP (depicted in stick model, hot pink C atoms) into HSA (PDB ID 2BXG) (chain A), depicting the best (lowest energy ranking) pose. (Upper part) Target protein is illustrated as cartoon with sub-domains color-coded according to chainbow. (Lower part) Ligand-binding site interactions of complex **2** (represented in semitransparent sphere model, magenta C atoms) docked onto HSA target protein (PDB ID 2BXG) (chain A). Yellow dotted lines indicate hydrogen bond, polar and hydrophobic interactions between the docked molecule and the amino acid residues (rendered in stick model and colored according to chainbow) of the binding pocket. Hydrogen atoms are omitted for clarity. The final structure was ray-traced. Interacting contacts are shown in Table S3.

compared to that of complex **1** (−34.57 kcal/mol compared to −13.10 kcal/mol) may be attributed to more hydrogen bonds and hydrophobic contacts of complex **2**, since the number of the interactions of a molecule inside the binding pocket plays important role in its stabilization inside the macromolecule. Our models for predicted binding poses of complexes **1** and **2** into CT DNA suggest intercalation of complexes with A and B helices of DNA, between purines and pyrimidines of the same strand and between strands as well, in major and minor grooves, respectively. Due to different domain of the DNA taking place in the binding of complexes **1** and **2**, no common nucleotide was found for the two molecules.

3.4.3. Docking calculations on human estrogen receptor alpha crystal structure

Given the cytotoxic activity of complexes **1** and **2** on MCF-7 estrogen receptor positive breast cancer cells expressing human estrogen receptor alpha (hERa) [10], it is interesting to examine if this activity is connected, or can be attributed, at least in part, to binding capacity of complexes **1** and **2** on hERa, a well-known target in breast cancer chemotherapy, since hormone receptor-positive breast cancers need estrogen and/or progesterone to grow. To this end, molecular docking calculations were employed to evaluate the ability of complexes **1** and **2** to bind in the crystal structure of hERa with bound co-crystallized 4-hydroxytamoxifen (OHT, PDB ID Nr 3ERT) (a drug used in breast cancer therapy by blocking the effects of estrogens in breast tissue), and estradiol (EST, PDB ID Nr 1A52) [76,77]. Complex **2** exhibited better cytotoxic activity than complex **1** on MCF-7 cells with IC_{50} values 38.1 μM and 70.2 μM, respectively [10]. It is interesting to notice that human breast hormone-dependent MCF-7 cells were almost two times more sensitive to complex **2**, than to complex **1**. The better cytotoxic activity of complex **2** could be explained, if a better binding of complex **2** on hERa, compared to complex **1**, could be demonstrated with the aid of *in silico* molecular docking studies. The binding energies for the best docking poses are illustrated in Table 4. Better binding capacity (lower binding energy) with hERa was documented for complex **2** (binding energies −25.66 kcal/mol and −34.52 kcal/mol, for ERa with PDB ID's: 1a52 and 3ert, respectively), compared to that of complex **1** (binding energies −17.24 kcal/mol and −12.98 kcal/mol, for ERa with PDB ID: 1a52 and 3ert, respectively). Complexes **1** and **2** were stabilized inside a pocket in the ligand-binding domain (LBD) of hERa (hERa-LBD). From Fig. 11, it is obvious that the less bulky complex **2** was stabilized inside the ligand-binding cavity of hERa exactly at the pocket where the co-crystallized molecules EST and OHT are bound, while complex **1** was anchored in an adjacent binding position to that of the ER modulators. Detected lower energy conformation for the docking of complex **2** compared to that of complex **1**, along with better stabilization of complex **2** deeper in the crevice of hERa-LBD, at the same place occupied by OHT and EST (sharing also common binding amino acid residues) may in part explain the better cytotoxic activity of complex **2** on MCF-7 human breast cancer cells [10].

3.4.4. Docking calculations on cancer-related target proteins

Since mononuclear complex **2** presented promising cytotoxic activity which is superior to that of the corresponding hexanuclear complex **1** as well as of Hmef and H_2sao, for all cell lines tested [10], *in silico* molecular docking simulations were employed to render a molecular basis for the understanding of this activity, through study of the binding capacity of complex **2** on a variety of target proteins implicated in cancer growth. This approach, which is a typical structure based target prediction taking into account the structure of a protein, involves the concept of inverse docking: whereby single molecule docked against panel of target protein structures followed by sorting/ranking of the proteins depending upon binding free energy of compound. Typically, molecule in question is docked to the active site of set of target proteins and depending on docking score and interaction pattern, target is assigned to the molecule in a specific order (ranking).

Reverse docking can be used to discover new targets for existing drugs and natural compounds, explain polypharmacology and the molecular mechanism of a substance, find alternative indications of drugs through drug repositioning, and detecting adverse drug reactions and drug toxicity [78]. The proteins identified in this study might include both direct targets and downstream regulated proteins. Proteins that can directly bind to the studied compound might be considered as possible direct targets of this compound. From Fig. S7, it is deduced that complex **2** is bound in each crystal structure in the ligand-binding site of the protein and in most cases exactly at the same place occupied by its co-crystallized complexed inhibitor, giving insights in the possible role of this compound in anticancer therapy. The results suggested that the following proteins: carbonic anhydrase II, cyclin-dependent kinase 2 (CDK2), 17beta-Hydroxysteroid Dehydrogenase Type 1, human galectin-3, lymphocyte-specific kinase (Lck), spleen tyrosine kinase (Syk), protein kinase C theta (PKC-theta), extracellular signal-regulated kinase

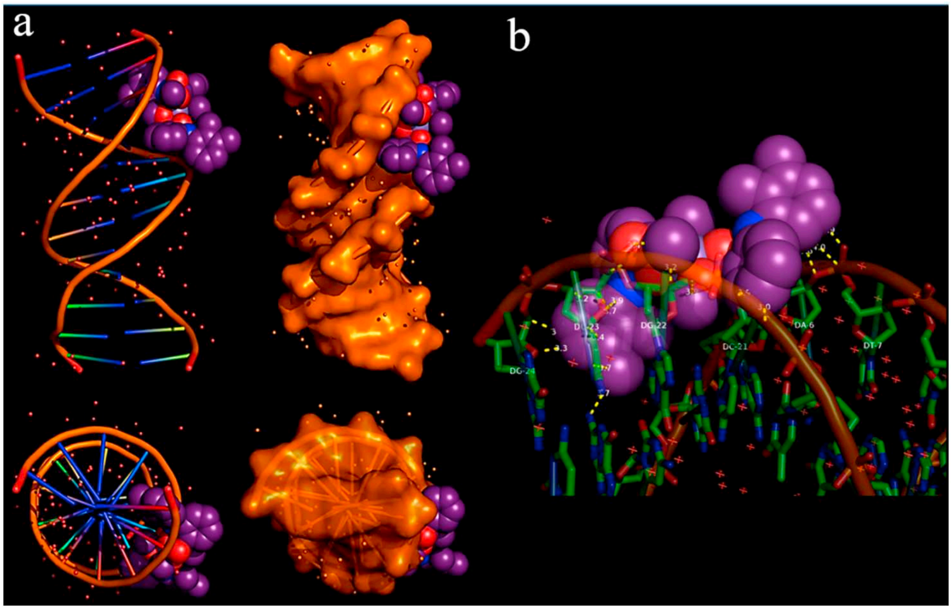

Fig. 9. (a) Molecular docking of complex **2** (rendered in sphere model, magenta C atoms) in the crystal structure of CT DNA (PDB ID 1BNA) in the binding cavity of minor groove of DNA. DNA structure is illustrated as cartoon color-coded according to chain (left) or opaque (upper part) and semitransparent (lower part) surface in brown color (right). In lower part, the docking pose from a view above the axis of the helix is illustrated. (b) Ligand-binding site interactions of complex **2** in the crystal structure of CT DNA (PDB ID 1BNA). Nucleotide molecules (labeled in white) are rendered in semi-transparent stick model and colored in green C atoms. Yellow dotted lines indicate hydrogen bond, polar and hydrophobic interactions between the docked molecule and the nucleotides of the binding pocket in the minor groove of DNA. Hydrogen atoms of all molecules are omitted for clarity. Atoms are numbered according to PyMol software. The final structure was ray-traced. Interacting contacts are shown in Table S4.

(ERK2), aldose reductase (AR), phosphatidylinositol 3-kinase (PI3K alpha), p38 mitogen-activated kinase and Janus kinase 3 (Jak3) tyrosine-protein kinase, might play important roles in the cytotoxicity mechanism of complex **2**. Several of these proteins can modulate significant nodes in various intracellular signal transduction pathways correlated to cancer growth.

Two of these proteins were chosen to be further discussed due to their expression pattern in previously studied cell lines. It is interesting to notice that some of these proteins may have multiple functions and play important roles in more than one pathway like cell proliferation/cell death and carcinogenesis. CDK2 protein (PDB ID 1h07) was chosen as a target protein, since MCF-7 cell line which was found to be sensitive to complex **2** [10], expresses the cyclin-dependent kinase inhibitor 2A (CDKN2A) tumor suppressor gene, encoding three splice variants, two of which serve as inhibitors of the cyclin-dependent kinase 4 (CDK4) and are capable of inducing arrest at the G1 phase of the cell cycle [79]. In human cancer cell lines derived from various tumor types, a high frequency of genetic and epigenetic alterations (*e.g.* promoter hyper-methylation, homozygous deletion or mutation) in the CDKN2A gene has been observed. Accordingly, epigenetic/genetic modulation of changes in CDKN2A might be a promising strategy for prevention or therapy of cancer. Furthermore, changes in CDKN2A status are highly variable depending on the type of cancer. In addition to skin cancer such as melanoma, changes of CDKN2A have been described in a wide spectrum of cancer types, such as non-small cell lung carcinoma (NSCLC) [80]. Since MCF-7 and A549 NSCLC cells express the mutated form of CDKN2A, they cannot express this type of tumor suppressor gene which could play a crucial role in inducing arrest at the G1 phase of the cell cycle. This is why MCF-7 cells do not encode splice variants which can serve as inhibitors of the CDK4 kinase. In MCF-7 cells, this deficiency in the inhibition pathway can be bypassed, when other CDK4 kinase inhibitors are administered. Complex **2** has been shown to act as a CDK2/4 inhibitor (Fig. S7), contributing in this way to the cell cycle arrest and leading cancer cells to an apoptotic pathway.

The PI3K pathway is the most frequently enhanced oncogenic pathway in breast cancer. The phosphatidylinositol-4,5-bisphosphate 3-kinase catalytic subunit alpha (PIK3CA) gene encodes the p110α catalytic subunit of PI3K. Among mechanisms of PI3K enhancement, PIK3CA mutations are most frequently observed, along with protein loss of phosphatase and tensin homolog (PTEN) [81,82]. PI3K operates as part of

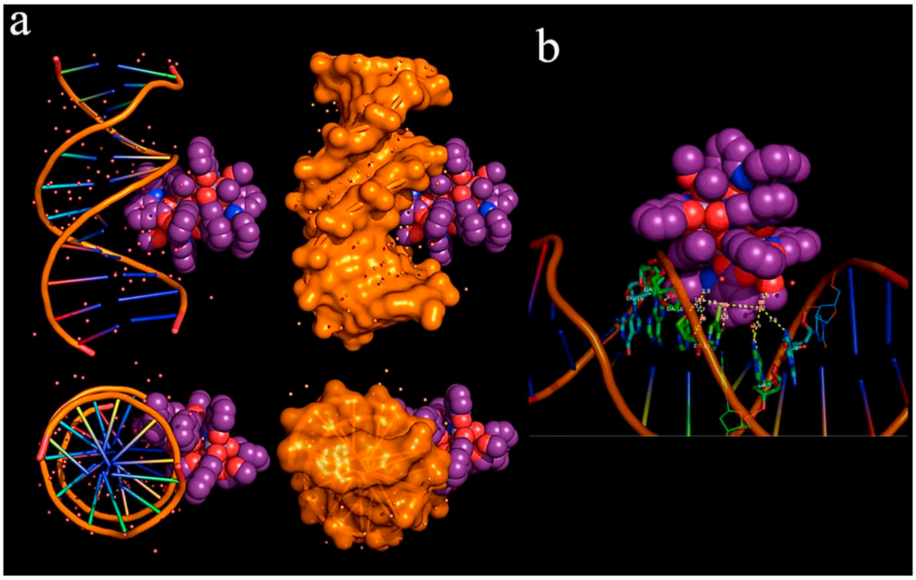

Fig. 10. (a) Molecular docking of complex **1** (rendered in sphere model, magenta C atoms) in the crystal structure of CT DNA (PDB ID 1BNA) in the binding cavity of major groove of DNA. DNA structure is illustrated as cartoon color-coded according to chain (left) or opaque (upper part) and semi-transparent (lower part) surface in brown color (right). In lower part, the docking pose from a view above the axis of the helix is illustrated. (b) Ligand-binding site interactions of complex **1** in the crystal structure of CT DNA (PDB ID 1BNA). Nucleotide molecules (labeled in white) are rendered in semi-transparent stick model and colored according to chain (in green and light blue C atoms). Yellow dotted lines indicate hydrophobic interactions and an extended hydrogen bond network between the docked molecule and the nucleotides of the binding pocket in the major groove of DNA. Hydrogen atoms of all molecules are omitted for clarity. Atoms are numbered according to PyMol software. The final structure was ray-traced. Interacting contacts are shown in Table S5.

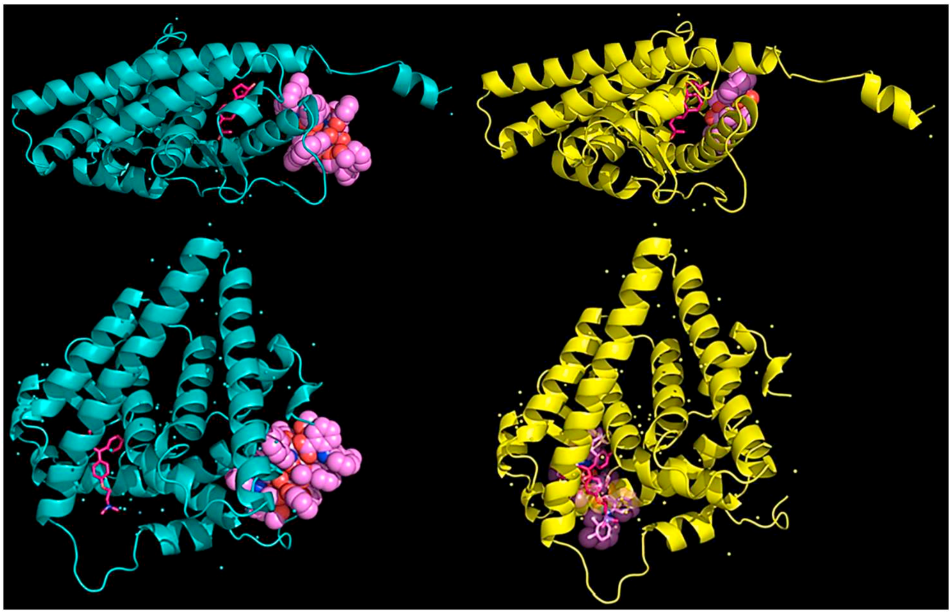

Fig. 11. Docking poses of complexes **1** (left part) and **2** (right part) on crystal structure of hERa: PDB ID 1a52 (upper part) and PDB ID 3ert (lower part). In the structure, the superimposed molecules EST (upper part) and OHT (lower part) are also shown. Target protein is illustrated as cartoon, while superimposed docked molecules represented either in sphere model colored according to atom type in light pink C atoms (complexes **1** and **2**), or in stick model colored according to atom type in hot pink C atoms (OHT and EST). Complex **2** (in lower right part) is depicted as semitransparent spheres for visibility reasons, since it is superimposed with OHT at the same binding site. Hydrogen atoms are omitted for clarity. The final structure was ray-traced.

the PI3K/Protein Kinase B (PKB)/mammalian target of rapamycin (PI3K/AKT/mTOR) pathway to mediate cell proliferation, survival, migration and vesicular trafficking, and mutations in PIK3CA have been implicated in several cancers including those arising from colon, lung, ovary, and breast. PI3Ks play a pivotal role in cell metabolism and proliferation, affecting both cancer and metabolic disorders [83–85]. PIK3CA mutations represent one of the most common genetic aberrations in breast cancer. They have been reported to be present in over one-third of cases, with enrichment in the luminal and in human epidermal growth factor receptor 2-positive subtypes. PIK3CA mutations are most likely to be observed in ER-positive/HER2-negative tumors, such as MCF-7 cells. However, several characteristics of PIK3CA mutations in breast cancer have been observed, including a strong association with expression of the estrogen receptor (ER). Several studies have demonstrated a clear synergy between endocrine treatment and various PI3K blocking agents [86,87]. PIK3CA-mutated NSCLC represents a clinically and genetically heterogeneous subgroup in adenocarcinomas [88]. In NSCLC, mutations within PIK3CA are considered oncogenic and targetable [89,90]. PI3K-inhibitors have not been yet proven to be clinically effective, at least in lung cancer, in the majority of patients with PIK3CA-mutation [89]. Finally, regulation of these proteins by complex **2** might cause a change of metabolism and survival status in human cancer cells that have been previously proved to be sensitive to this complex [10].

3.5. PASS biological activity prediction profile

Prediction of activity spectra is based on PASS technology which can predict over 4,000 kinds of biological activity, including pharmacological effects, mechanisms of action, toxic and adverse effects, interaction with metabolic enzymes and transporters, influence on gene expression, *etc.* [45].

3.5.1. Activity spectra prediction

The results for activity spectra prediction for complex **2** with Pa > 0.7 are reported in Table S6. It is interesting to note that the two first places in the ranking are occupied for anti-inflammatory and analgesic drug activity, maybe due to the NSAID mefenamato moiety of the complex.

3.5.2. Quantitative prediction of antitarget interaction profiles

Quantitative predictions of the interaction of complex **2** with antitarget proteins by GUSAR software [46] are shown in Table S7. The antitarget prediction profile showed that complex **2** falls in the applicability domain for estrogen receptor antagonist activity, which was also documented by docking calculations on hERa crystal structure.

3.5.3. Prediction of drug-induced changes of gene expression

The DIGEP-Pred of drug-induced changes of gene expression profile [49] for complex **2** is shown in Tables S8–S13. The tables illustrate the propability data (in terms of Pa and Pi values) from prediction results for complex **2** based on mRNA, protein, MCF-7 human breast cells, VCaP 6 h (VCaP prostate cancer cells), VCaP 24 h and the combination prediction results, respectively. The more probable changes of gene expression are at the top of the list. Only the down-regulated and up-regulated target proteins predicted with a Pa > 0.5 are shown. From Table S8 it is interesting to notice that the first entry with the highest Pa value (0.937) in the mRNA-based training set prediction of 500 up-regulation genes is 15-hydroxyprostaglandin dehydrogenase (HPGD or 15-PGDH).

It is known that down-regulation of the expression of 15-PGDH in lung and other tumors suggests that this enzyme is a tumor suppressor. Yan et al. discovered that the median expression of 15-PGDH in colon tumor samples was at least 17-fold below the median expression in normal colon [91]. Similarly, Backlund et al. found that 15-PGDH is down-regulated in colorectal as well in other cancers using activity and microarray analysis [92]. Furthermore, Wolf et al. also described that 15-PGDH is under-expressed in primary breast tumors [93]. Due to expression status of 15-PGDH in various tumors, a number of anticancer agents, such as transforming growth factor-β1 (TGF-β1), glucocorticoids and some histone deacetylase inhibitors (HDACs), were found to exert an up-regulated activity, leading to induction of 15-PGDH expression. It has been shown that over-expression of 15-PGDH in A549 cells resulted in apoptosis [94]. These results suggest that tumor suppressive action of complex **2** documented in previous report [10] may, in part, be related to its ability to induce 15-PGDH expression. In this way, complex **2** could exhibit its action as anticancer therapeutic, at least in part, by inducing the expression (up-regulation) of tumor suppressive 15-PGDH gene. In Table S9 showing the protein-based prediction results, it is revealed that complex **2** is able to down-regulate CD62 antigen-like family member L protein with a probability value of 0.806. In the past, many studies were focused on the role of selectin L as a mediator of tumor cell adhesion and extravasation during metastasis [95]. Up-regulated expression of CD62L was observed by flow cytometric analysis of freshly isolated tumor cells from biopsies of high grade cancer specimens.

In addition, *in silico* analysis of Oncomine Microarray Database showed a significant correlation between CD62L expression and tumor aggressiveness and clinical outcomes. This down-regulated activity of complex **2** may alleviate the CD62L-overexpressed influence on cell tumor proliferation. In Table S10, the down-regulated activity of complex **2** on DEK proto-oncogene is illustrated with a probability value of 0.631. DEK oncogene is a target of steroid hormone receptor signaling in breast cancer [96]. Previously, it has been shown that the DEK oncogene, which is a chromatin remodeling protein, supports breast cancer cell proliferation, invasion and the maintenance of the breast cancer stem cell population. DEK expression is associated with positive hormone receptor status in primary breast cancers and is up-regulated *in vitro* following exposure to the hormones estrogen, progesterone, and androgen. DEK is a novel ERα target gene whose expression promotes estrogen-induced proliferation. DEK protein levels are elevated in both MCF-7 cultured cells and primary invasive adenocarcinomas and that DEK expression stimulates breast cancer cell proliferation *in vitro* [97]. In addition, it was found that DEK isoform 1 was expressed in HeLa cells [98] and DEK exhaustion inhibited the growth of A549 cells [99].

Down-regulation of DEK oncogene by complex **2** may act synergistically on its antiestrogen activity. Since expression of estrogen and progesterone hormone receptors indicates a favorable prognosis due to the successful use of hormonal therapies such as tamoxifen and aromatase inhibitors, targeted inhibition of DEK by complex **2** may enhance the efficacy of conventional hormone therapies in ER(+) breast tumors. The previously reported cytotoxic activity of complex **2** on MCF-7, HeLa and A549 cells [10] may, in part, be explained by the induction of DEK oncogene down-regulation by this compound.

3.5.4. Sites of metabolism prediction

For the prediction of SOMPs [50] for complex **2**, sets for the five isoforms of CYP P450 that metabolize the majority of xenobiotics have been prepared: 3A4, 2C9, 2C19, 2D6 and 1A2. The reaction of glucoronidation was also included, which is catalyzed by UGT (Fig. S8). In Fig. S8 the SoLAs are illustrated, in which labeled atom is a SOM with positive ΔP values. The labeled atoms in SOM (ΔP+) revealed to be 10, 6, 8, 11, 10 and 6 atoms of complex **2** for CYP3A4, CYP2D6, CYP2C19, CYP2C9, CYP1A2 and UGT, respectively.

3.5.5. Polypharmacology browser for target prediction in ChEMB

PPB for target prediction approach uses the ChEMBL Database (containing information of drug-like bioactive compounds) [51], which is a publicly available database and collects the information on biologically active molecules reported in literature. As of now, PPB contains 1.6 million distinct compounds reported and > 10,000 target proteins. With PPB we explored the ability of complex **2** to interact with more than one target proteins. Target identification has become an area of intense research owing to widespread application ranging from the identification of the biologically active molecule, drug re-purposing, toxicity prediction to the identification of promiscuous drugs or compounds (Poly-Pharmacology). Interactions of the drug molecule with unintended side targets (off-targets) often leads to adverse drug reactions and it is shown to be one of the most common reasons for the failure of drug molecule in the clinical trials. The poly-pharmacology profile of complex **2** identifying probable target proteins is illustrated in Table S14. From Table S14, it is deduced that P = 0 only for 4 and 6 ChEMBL-IDs targets retrieved from fingerprints Sfp and ECfp4 with ChEMBL-names AKR1B10, AKR1C1, AKR1C3, ACHE and PTGS2.

3.5.6. PharmMapper target protein identification

PharmMapper is an *in silico* pharmacophore-based reverse screening tool that attempts to identify potential target candidates for small-molecule drugs, natural products or novel compounds whose targets are unknown [100]. Drug target identification of complex **2** by means of pharmacophore mapping approach is shown in Table S15. From a total of 198 pharmacophore entry predictions, it is interesting to notice that serum albumin is displayed in 13th place. The 6th place is occupied by Phospholipase A2 (PLA2) isoform 1. PLA2 is the initial enzyme of arachidonic acid cascade, having key-role in inflammation and cancer [101]. Binding of sPLA2-IB/PLA2G1B induces various effects depending on the cell type, such as activation of the mitogen-activated protein kinase (MAPK) cascade to induce cell proliferation, the production of lipid mediators, selective release of arachidonic acid in bone marrow-derived mast cells. In neutrophils, binding of sPLA2-IB/PLA2G1B can activate p38 MAPK to stimulate elastase release and cell adhesion. Since PLA2 inhibitors have wide medicinal importance, PharmMapper target protein prediction revealed the possibility of the utility of complex **2** as anti-inflammatory and anticancer agent.

3.5.7. Antitargets prediction and identifying drug repositioning potential and adverse drug reactions via the chemical-protein interactome

The drug repositioning potential and adverse drug reactions (DRAR) *via* the chemical-protein interactome (CPI), (DRAR-CPI), [57] is a server for predicting DRAR. In this study, without mining the microarray data, we demonstrated the power of CPI to represent the perturbation towards the biosystems and how it would be used in measuring drug effect. We have examined the possible therapeutic indications or ADRs of complex **2** based on positive or negative association scores between complex **2** and a library of drugs based on their interaction profiles towards the targets. Associations of library of drugs towards complex **2** are shown in Table S16 (the first 60 from total 1,200 associations are shown). The results are ranked by association scores and the corresponding P values, according to similarity (or disparity) with known indications and ADR information suggesting in this way new indications and ADRs. Positive association was revealed with drugs: indinavir, irinotecan, butorphanol, methacycline, idarubicin, aliskiren, cabergoline, netilmicin, nalbuphine, ergoloid mesylate, lapatinib, lymecycline, epirubicin, minocycline, doxycycline, demeclocycline, daunorubicin, tobramycin, buprenorphine, acarbose and buprenorphine, for the treatment of pain, various infections and cancer, among others. These data should be confirmed by specific *in vitro* experiments.

4. Conclusions

In continuation to our reported research regarding the structural, magnetochemical and spectroscopic properties and the cytotoxic activity of complexes $[Mn_6(O)_2(mef)_2(sao)_6(CH_3OH)_4]$ **1**, and $[Mn(mef)_2(CH_3OH)_4]$ **2** [10], we have studied the *in vitro* and *in silico* interaction of the complexes with CT DNA, BSA and HSA and possible interaction with other protein targets involved in various diseases, and have compared them with those of the free ligands.

The complexes can bind tightly to CT DNA by intercalation as indicated by UV–vis spectroscopy, viscosity measurements and competitive binding studies with the classical intercalator EB. The complexes can also bind tightly and reversibly to the albumins BSA and HSA as shown by the SA-binding constants which are in an optimum range to confirm the binding of the complexes, their transportation by the SAs and their possible release upon arrival at their biological targets.

The results from the present molecular modeling simulations may provide useful complementary insights for the elucidation of the mechanism of action of the studied complexes at a molecular level [41]. *In silico* procedures indicate better activity of complex **2** than that of complex **1**. Furthermore, both *in vitro* and *in silico* studies revealed a role for complex **2** in human breast cancer cells, acting as an estrogen receptor alpha (hERa) antagonist, and also as a down-regulator for DEK proto-oncogene, a novel estrogen receptor α (ERα) target gene whose expression promotes estrogen-induced proliferation. Further *in silico* studies adopting various procedures contributed in the understanding of the role of complex **2** in various diseases, suggesting a mode of action of this compound.

Molecular modeling calculations can provide a molecular basis for the understanding of both the impairment of DNA by its binding with the studied complexes and also the ability of these compounds for transportation through blood serum albumin and possible interaction with other protein targets involved in various diseases. This study can provide information for the elucidation of the mechanism of action of both complexes in a molecular level [41].

Docking studies contributed in better understanding the binding interactions of the tested complexes within the active site of the studied proteins and DNA. Furthermore, *in silico* prediction of the activity of complex **2** contributed in the elucidation of its *in vitro* activity and shed light in possible interaction with various macromolecules involved in many diseases and especially cancer. It is necessary to keep in mind that the predictive tools used provide the qualitative estimation of the synthesized complex activity, calculating the probability of belonging to the classes of “actives” and “inactives”, respectively. Therefore, it is necessary not just to confirm that complex **2** is active in the experimental assay but also to determine the extent of its potency. If, for example, adverse or toxic effects are predicted for this compound, this is an indication that the compound under study has some structural similarity with the compounds from the training set with those effects. However, it should be determined experimentally if adverse or toxic effects arise at the same dose/concentration as the desirable pharmacotherapeutic action, or much higher doses. Also, it is necessary to keep in mind that prediction for adverse and toxic effects is based on clinical manifestations, which are sometimes observed in a few or even in a single patient. Finally, due to wide range of predicted biological activity spectrum, it should be more interesting to prioritize the selection for *in vitro* testing of these activities based on those with the highest probability.

Abbreviations

15-PGDH	15-hydroxyprostaglandin dehydrogenase
ADR	adverse reaction
APfp	Atom-Pair fingerprint
AR	aldose reductase
AUC	area under the ROC curve
BSA	bovine serum albumin
CDK2	cyclin-dependent kinase 2
CDK4	cyclin-dependent kinase 4
CDKN2A	cyclin-dependent kinase inhibitor 2A
CPI	chemical-protein interactome
CT	calf-thymus
CTD	Comparative Toxicogenomics Database
DIGEP-Pred	Drug-Induced Gene Expression Profiles Prediction
DMSO	dimethylsulfoxide
DRAR	drug repositioning and adverse reaction
DRAR-CPI	repositioning potential and adverse drug reactions (DRAR) *via* the chemical-protein (CPI)
EB	ethidium bromide, 3,8-diamino-5-ethyl-6-phenyl-phenanthridinium bromide
ECfp4	Extended-connectivity fingerprint
ER	estrogen receptor
ERK2	extracellular signal-regulated kinase
EST	estradiol
H_2sao	salicylaldoxime
HDACs	histone deacetylase inhibitors
hERa	human estrogen receptor alpha
Hmef	mefenamic acid, 2-(2,3-dimethylphenylamino)benzoic acid, *N*-(2,3-xylyl)anthranilic acid
HSA	human serum albumin
IAP	Invariant Accuracy of Prediction
IBP	ibuprofen, 2-(4-isobutylphenyl)propionic acid
IC_{50}	50% inhibitory concentration
Jak3	Janus kinase 3
K	SA-binding constant
K_b	DNA-binding constant
k_q	quenching constant
K_{SV}	Stern-Volmer constant
LBD	Ligand-binding domain
Lck	lymphocyte-specific kinase
LMNA	Labelled Multilevel Neighbourhoods of Atoms
MAPK	mitogen-activated protein kinase
MC	metallacrown
mef^{1-}	anion of mefenamic acid
MQN	Molecular Quantum Numbers
mTOR	mammalian target of rapamycin
NSAID	non-steroidal anti-inflammatory drug
NSCLC	non-small cell lung carcinoma
O_{cent}	encapsulated oxygen
OHT	4-hydroxytamoxifen
O_{ox}	oximato oxygen
O_{sal}	salicylato oxygen
Pa	probability “to be active”
PASS	Prediction of activity spectra for substances
PDB	Protein Data Bank
Pi	probability “to be inactive”
PI3K alpha	phosphatidylinositol 3-kinase
PIK3CA	phosphatidylinositol-4,5-bisphosphate 3-kinase catalytic subunit alpha
PKB	Protein Kinase B
PKC-theta	protein kinase C theta
PLA2	Phospholipase A2
PPB	polypharmacology browser
PTEN	phosphatase and tensin homolog
QSAR	quantitative structure-activity relationship
ROC	receiver operating characteristic
SA	serum albumin
sao^{2-}	dianion of salicylaldoxime
SDF	structure data file
Sfp	Substructure fingerprint
SMIfp	SMILES fingerprint
SMILES	simplified molecular-input line-entry system
SoLAs	structures with one labeled atom
SOM	site of metabolism
SOMP	sites of metabolism prediction
Syk	spleen tyrosine kinase
TGF-β1	transforming growth factor-β1
Xfp	Topological Pharmacophore fingerprint
λ_{exc}	excitation wavelength
λ_{em}	emission wavelength
τ_o	fluorescence lifetime

Appendix A. Supplementary data

Supplementary data to this article can be found online at https://doi.org/10.1016/j.jinorgbio.2018.09.017.

References

[1] J.E. Weder, C.T. Dillon, T.W. Hambley, B.J. Kennedy, P.A. Lay, J.R. Biffin, H.L. Regtop, N.M. Davies, Coord. Chem. Rev. 232 (2002) 95–126.
[2] J.E.F. Reynolds, W. Martindale, The Extra Pharmacopoeia, 31st ed., The Pharmaceutical Press, London, 1996.
[3] D.M. Boothe, H.R. Adams (Ed.), Veterinary Pharmacology and Therapeutics, 8th ed., Iowa State University Press, Ames, IA, 2001, pp. 433–435.
[4] T. Pringsheim, W.J. Davenport, D. Dodick, Neurology 70 (2008) 1555–1563.
[5] F. Dimiza, A.N. Papadopoulos, V. Tangoulis, V. Psycharis, C.P. Raptopoulou, D.P. Kessissoglou, G. Psomas, Dalton Trans. 39 (2010) 4517–4528.
[6] G. Facchin, M.H. Torre, E.J. Baran, Z. Naturforsch. B 53 (1998) 871–874.
[7] R.P. Sharma, S. Kumar, P. Venugopalan, V. Ferretti, A. Tarushi, G. Psomas, M. Witwicki, RSC Adv. 6 (2016) 88546–88558.
[8] F. Dimiza, S. Fountoulaki, A.N. Papadopoulos, C.A. Kontogiorgis, V. Tangoulis, C.P. Raptopoulou, V. Psycharis, A. Terzis, D.P. Kessissoglou, G. Psomas, Dalton

Trans. 40 (2011) 8555–8568.
[9] J. Feng, X. Du, H. Liu, X. Sui, C. Zhang, Y. Tang, J. Zhang, Dalton Trans. 43 (2014) 10930–10939.
[10] A. Tarushi, G.D. Geromichalos, K. Lafazanis, C.P. Raptopoulou, V. Psycharis, N. Lalioti, A.A. Pantazaki, D.P. Kessissoglou, V. Tangoulis, G. Psomas, New J. Chem. 42 (2018) 6955–6967.
[11] X. Totta, A.A. Papadopoulou, A.G. Hatzidimitriou, A. Papadopoulos, G. Psomas, J. Inorg. Biochem. 145 (2015) 79–93.
[12] V. Dokorou, Z. Ciunik, U. Russo, D. Kovala-Demertzi, J. Organomet. Chem. 630 (2001) 205–214.
[13] A. Tarushi, Z. Karaflou, J. Kljun, I. Turel, G. Psomas, A.N. Papadopoulos, D.P. Kessissoglou, J. Inorg. Biochem. 128 (2013) 85–96.
[14] E.J. Larson, V.L. Pecoraro, V.L. Pecoraro (Ed.), Manganese Enzymes, VCH Publishers Inc., New York, 1992, pp. 1–28.
[15] C.S. Mullins, V.L. Pecoraro, Coord. Chem. Rev. 252 (2008) 416–443.
[16] B. Chiswell, E.D. McKenzie, L.F. Lindoy, 41. Manganese, in: G. Wilkinson (Ed.), Comprehensive Coordination Chemistry, 4 Pergamon Press, Oxford, 1987, pp. 1–122.
[17] D.C. Weatherburn, S. Mandal, S. Mukhopadhyay, S. Bhaduri, L.F. Lindoy, 5.1 Manganese, in: J.A. McCleverty, T.J. Meyer (Eds.), Comprehensive Coordination Chemistry II, 5 Elsevier, 2003, pp. 1–125.
[18] Z. Guo, P.J. Sadler, Angew. Chem. Int. Ed. 38 (1999) 1512–1531.
[19] P. Dorkov, I. Pantcheva, W. Sheldrick, H. Figge, R. Petrova, M. Mitewa, J. Inorg. Biochem. 102 (2008) 26–32.
[20] M. Zampakou, M. Akrivou, E.G. Andreadou, C.P. Raptopoulou, V. Psycharis, A.A. Pantazaki, G. Psomas, J. Inorg. Biochem. 121 (2013) 88–99.
[21] M. Zampakou, S. Balala, F. Perdih, S. Kalogiannis, I. Turel, G. Psomas, RSC Adv. 5 (2015) 11861–11872.
[22] M. Li, C. Chen, D. Zhang, J. Niu, B. Ji, Eur. J. Med. Chem. 45 (2010) 3169–3177.
[23] D. Zhou, Q. Chen, Y. Qi, H. Fu, Z. Li, K. Zhao, J. Gao, Inorg. Chem. 50 (2011) 6929–6937.
[24] X. Chen, L. Tang, Y. Sun, P. Qiu, G. Liang, J. Inorg. Biochem. 104 (2010) 1141–1147.
[25] D.P. Singh, K. Kumar, C. Sharma, Eur. J. Med. Chem. 45 (2010) 1230–1236.
[26] M. Zampakou, N. Rizeq, V. Tangoulis, A.N. Papadopoulos, F. Perdih, I. Turel, G. Psomas, Inorg. Chem. 53 (2014) 2040–2052.
[27] M. Zampakou, A.G. Hatzidimitriou, A.N. Papadopoulos, G. Psomas, J. Coord. Chem. 68 (2015) 4355–4372.
[28] M. Zampakou, V. Tangoulis, C.P. Raptopoulou, V. Psycharis, A.N. Papadopoulos, G. Psomas, Eur. J. Inorg. Chem. (2015) 2285–2294.
[29] A. Tarushi, A.G. Hatzidimitriou, M. Estrader, D.P. Kessissoglou, V. Tangoulis, G. Psomas, Inorg. Chem. 56 (2017) 7048–7057.
[30] P. Tsiliki, F. Perdih, I. Turel, G. Psomas, Polyhedron 53 (2013) 215–222.
[31] K. Gurova, Future Oncol. 5 (2009) 1685–1704.
[32] U. Pindur, M. Jansen, T. Lemster, Curr. Med. Chem. 12 (2005) 2805–2847.
[33] L. Strekowski, B. Wilson, Mutat. Res. 623 (2007) 3–13.
[34] K.E. Erkkila, D.T. Odom, J.K. Barton, Chem. Rev. 99 (1999) 2777–2795.
[35] A.C. Komor, J.K. Barton, Chem. Commun. 49 (2013) 3617–3630.
[36] B.M. Zeglis, V.C. Pierre, J.K. Barton, Chem. Commun. (2007) 4565–4579.
[37] B.P. Esposito, R. Najjar, Coord. Chem. Rev. 232 (2002) 137–149.
[38] T. Zhang, T. Otevrel, Z.Q. Gao, Z.P. Gao, S.M. Ehrlich, J.Z. Fields, B.M. Boman, Cancer Res. 61 (2001) 8664–8667.
[39] C.N. Banti, S.K. Hadjikakou, Eur. J. Inorg. Chem. (2016) 3048–3071.
[40] G. Psomas, D.P. Kessissoglou, Dalton Trans. 42 (2013) 6252–6276.
[41] G.D. Geromichalos, A. Tarushi, K. Lafazanis, A.A. Pantazaki, D.P. Kessissoglou, G. Psomas, J. Inorg. Biochem. 187 (2018) 41–55.
[42] J. Marmur, J. Mol. Biol. 3 (1961) 208–211.
[43] M.F. Reichmann, S.A. Rice, C.A. Thomas, P. Doty, J. Am. Chem. Soc. 76 (1954) 3047–3053.
[44] V. Poroikov, D. Akimov, E. Shabelnikova, D. Filimonov, SAR QSAR Environ. Res. 12 (2001) 327–344.
[45] D.A. Filimonov, A.A. Lagunin, T.A. Gloriozova, A.V. Rudik, D.S. Druzhilovskii, P.V. Pogodin, V.V. Poroikov, Chem. Heterocycl. Compd. 50 (2014) 444–457.
[46] A.V. Zakharov, A.A. Lagunin, D.A. Filimonov, V.V. Poroikov, Chem. Res. Toxicol. 25 (2012) 2378–2385.
[47] D. Filimonov, V. Poroikov, Y. Borodina, T. Gloriozova, J. Chem. Inf. Comput. Sci. 39 (1999) 666–670.
[48] A.V. Zakharov, M.L. Peach, M. Sitzmann, M.C. Nicklaus, J. Chem. Inf. Model. 54 (2014) 713–719.
[49] A. Lagunin, S. Ivanov, A. Rudik, D. Filimonov, V. Poroikov, Bioinformatics 29 (2013) 2062–2063.
[50] A. Rudik, A. Dmitriev, A. Lagunin, D. Filimonov, V. Poroikov, Bioinformatics 31 (2015) 2046–2048.
[51] https://www.ebi.ac.uk/chembl/.
[52] D. Rogers, M. Hahn, J. Chem. Inf. Model. 50 (2010) 742–754.
[53] L. Ruddigkeit, L.C. Blum, J. Reymond, J. Chem. Inf. Model. 53 (2012) 56–65.
[54] J. Schwartz, M. Awale, J. Reymond, J. Chem. Inf. Model. 53 (2013) 1979–1989.
[55] M. Awale, J. Reymond, J. Chem. Inf. Model. 54 (2014) 1892–1907.
[56] M. Awale, J. Reymond, Nucleic Acids Res. 42 (2014) 234–239.
[57] H. Luo, J. Chen, L. Shi, M. Mikailov, H. Zhu, K. Wang, L. He, L. Yang, Nucleic Acids Res. 39 (2011) W492–W498.
[58] T.J. Ewing, S. Makino, A.G. Skillman, I.D. Kuntz, J. Comput. Aided Mol. Des. 15 (2001) 411–428.
[59] M.L. Smith, G. Hawcroft, M.A. Hull, Eur. J. Cancer 36 (2000) 664–674.
[60] A. Inoue, S. Muranaka, H. Fujita, T. Kanno, H. Tamai, K. Utsumi, Free Radic. Biol. Med. 37 (2004) 1290–1299.
[61] A. Tarushi, C.P. Raptopoulou, V. Psycharis, C.K. Kontos, D.P. Kessissoglou, A. Scorilas, V. Tangoulis, G. Psomas, Eur. J. Inorg. Chem. (2016) 219–231.
[62] Q. Zhang, J. Liu, H. Chao, G. Xue, L. Ji, J. Inorg. Biochem. 83 (2001) 49–55.
[63] A.M. Pyle, J.P. Rehmann, R. Meshoyrer, C.V. Kumar, N.J. Turro, J.K. Barton, J. Am. Chem. Soc. 111 (1989) 3051–3058.
[64] G. Pratviel, J. Bernadou, B. Meunier, Adv. Inorg. Chem. 45 (1998) 251–262.
[65] A. Wolfe, G. Shimer, T. Meehan, Biochemistry 26 (1987) 6392–6396.
[66] A. Dimitrakopoulou, C. Dendrinou-Samara, A.A. Pantazaki, M. Alexiou, E. Nordlander, D.P. Kessissoglou, J. Inorg. Biochem. 102 (2008) 618–628.
[67] J.L. Garcia-Gimenez, M. Gonzalez-Alvarez, M. Liu-Gonzalez, B. Macias, J. Borras, G. Alzuet, J. Inorg. Biochem. 103 (2009) 923–934.
[68] J.R. Lakowicz, Principles of Fluorescence Spectroscopy, third ed., Plenum Press, New York, 2006.
[69] W.D. Wilson, L. Ratmeyer, M. Zhao, L. Strekowski, D. Boykin, Biochemistry 32 (1993) 4098–4104.
[70] G. Zhao, H. Lin, S. Zhu, H. Sun, Y. Chen, J. Inorg. Biochem. 70 (1998) 219–226.
[71] D.P. Heller, C.L. Greenstock, Biophys. Chem. 50 (1994) 305–312.
[72] C. Tan, J. Liu, H. Li, W. Zheng, S. Shi, L. Chen, L. Ji, J. Inorg. Biochem. 102 (2008) 347–358.
[73] V. Rajendiran, R. Karthik, M. Palaniandavar, H. Stoeckli-Evans, V.S. Periasamy, M.A. Akbarsha, B.S. Srinag, H. Krishnamurthy, Inorg. Chem. 46 (2007) 8208–8221.
[74] O.H. Laitinen, V.P. Hytonen, H.R. Nordlund, M.S. Kulomaa, Cell. Mol. Life Sci. 63 (2006) 2992–3017.
[75] S. Sugio, A. Kashima, S. Mochizuki, M. Noda, K. Kobayashi, Protein Eng. 12 (1999) 439–446.
[76] D.M. Tanenbaum, Y. Wang, S.P. Williams, P.B. Sigler, Proc. Natl. Acad. Sci. U. S. A. 95 (1998) 5998–6003.
[77] A.K. Shiau, D. Barstad, P.M. Loria, L. Cheng, P.J. Kushner, D.A. Agard, G.L. Greene, Cell 95 (1998) 927–937.
[78] M. Lee, D. Kim, BMC Bioinf. 13 (2012) S6.
[79] L.G. Aoude, K.A. Wadt, A.L. Pritchard, N.K. Hayward, Pigment Cell Melanoma Res. 28 (2015) 148–160.
[80] A. Marchetti, F. Buttitta, S. Pellegrini, G. Bertacca, A. Chella, V. Carnicelli, V. Tognoni, A. Filardo, C.A. Angeletti, J. Pathol. 181 (1997) 178–182.
[81] T. Mukohara, Breast Cancer 7 (2015) 111–123.
[82] D. Zardavas, W.A. Phillips, S. Loi, Breast Cancer Res. 16 (2014) 201.
[83] J.A. Engelman, J. Luo, L.C. Cantley, Nat. Rev. Genet. 7 (2006) 606–619.
[84] T. Yuan, L.C. Cantley, Oncogene 27 (2008) 5497–5510.
[85] K.D. Courtney, R.B. Corcoran, J.A. Engelman, J. Clin. Oncol. 28 (2010) 1075–1083.
[86] S. Massarweh, C.K. Osborne, C.J. Creighton, L. Qin, A. Tsimelzon, S. Huang, H. Weiss, M. Rimawi, R. Schiff, Cancer Res. 68 (2008) 826–833.
[87] S. Loi, B. Haibe-Kains, S. Majjaj, F. Lallemand, V. Durbecq, D. Larsimont, A.M. Gonzalez-Angulo, L. Pusztai, W.F. Symmans, A. Bardelli, P. Ellis, A.N. Tutt, C.E. Gillett, B.T. Hennessy, G.B. Mills, W.A. Phillips, M.J. Piccart, T.P. Speed, G.A. McArthur, C. Sotiriou, Proc. Natl. Acad. Sci. U. S. A. 107 (2010) 10208–10213.
[88] M. Scheffler, M. Bos, M. Gardizi, K. König, S. Michels, J. Fassunke, C. Heydt, H. Künstlinger, M. Ihle, F. Ueckeroth, K. Albus, M. Serke, U. Gerigk, W. Schulte, K. Töpelt, L. Nogova, T. Zander, W. Engel-Riedel, E. Stoelben, Y. Ko, W. Randerath, B. Kaminsky, J. Panse, C. Becker, M. Hellmich, S. Merkelbach-Bruse, L.C. Heukamp, R. Büttner, J. Wolf, Oncotarget 6 (2015) 1315–1326.
[89] G.R. Oxnard, A. Binder, P.A. Jänne, J. Clin. Oncol. 31 (2013) 1097–1104.
[90] S. Kang, A.G. Bader, P.K. Vogt, Proc. Natl. Acad. Sci. U. S. A. 102 (2005) 802–807.
[91] M. Yan, R.M. Rerko, P. Platzer, D. Dawson, J. Willis, M. Tong, E. Lawrence, J. Lutterbaugh, S. Lu, J.K. Willson, G. Luo, J. Hensold, H. Tai, K. Wilson, S.D. Markowitz, Proc. Natl. Acad. Sci. U. S. A. 101 (2004) 17468–17473.
[92] M.G. Backlund, J.R. Mann, V.R. Holla, F.G. Buchanan, H. Tai, E.S. Musiek, G.L. Milne, S. Katkuri, R.N. Dubois, J. Biol. Chem. 280 (2005) 3217–3223.
[93] I. Wolf, J. O'Kelly, T. Rubinek, M. Tong, A. Nguyen, B.T. Lin, H. Tai, B.Y. Karlan, H.P. Koeffler, Cancer Res. 66 (2006) 7818–7823.
[94] H. Tai, M. Tong, Y. Ding, Prostaglandins Other Lipid Mediat. 83 (2007) 203–208.
[95] D. Choudhary, P. Hegde, O. Voznesensky, S. Choudhary, S. Kopsiaftis, K.P. Claffey, C.C. Pilbeam, J.A. Taylor, Urol. Oncol. 33 (2015) 387.e17–387.e27.
[96] L.M. Privette Vinnedge, S. Ho, K.A. Wikenheiser-Brokamp, S.I. Wells, PLoS One 7 (2012) e46985.
[97] L.M. Privette Vinnedge, R. McClaine, P.K. Wagh, K.A. Wikenheiser-Brokamp, S.E. Waltz, S.I. Wells, Oncogene 30 (2011) 2741–2752.
[98] L. Yu, X. Huang, W. Zhang, H. Zhao, G. Wu, F. Lv, L. Shi, Y. Teng, Oncotarget 7 (2016) 26844–26855.
[99] J. Wang, L. Sun, M. Yang, W. Luo, Y. Gao, Z. Liu, X. Qiu, E. Wang, J. Histochem. Cytochem. 61 (2013) 510–521.
[100] X. Liu, S. Ouyang, B. Yu, Y. Liu, K. Huang, J. Gong, S. Zheng, Z. Li, H. Li, H. Jiang, Nucleic Acids Res. 38 (2010) W609–W614.
[101] N.S. Yarla, K. Satyakumar, D. Srinivasu, D.S.V.G.K. Kaladhar, G. Aliev, G. Dharmapuri, G.R.S.S. Putta, S. Jagarlapoodi, V. Bheeram, S.P. Sadu, G.R. Duddukuri, J. Cancer Sci. Ther. 7 (2015) 249–252.